

The Deflagration Stage of Chandrasekhar Mass Models For Type Ia Supernovae: I. Early Evolution

C. M. Malone¹, A. Nonaka², S. E. Woosley¹, A. S. Almgren², J. B. Bell², S. Dong¹,
M. Zingale³

ABSTRACT

We present high-resolution, full-star simulations of the post-ignition phase of Type Ia supernovae using the compressible hydrodynamics code Castro. Initial conditions, including the turbulent velocity field and ignition site, are imported directly from a simulation of the last few hours of presupernova convection using a low Mach number code, Maestro. Adaptive mesh refinement allows the initial burning front to be modeled with an effective resolution of $36,864^3$ zones (136 m zone^{-1}). The initial rise and expansion of the deflagration front are tracked until burning reaches the star's edge and the role of the background turbulence on the flame is investigated. The effect of artificially moving the ignition location closer to the star's center is explored. The degree to which turbulence affects the burning front decreases with increasing ignition radius since the buoyancy force is stronger at larger radii. Even central ignition — in the presence of a background convective flow field — is rapidly carried off-center as the flame is carried by the flow field. We compare our results to analytic models for burning thermals, and find that they reproduce the general trends of the bubble's size and mass, but underpredict the amount of buoyant acceleration due to simplifying assumptions of the bubble's properties. Overall, we find that the amount of mass that burns prior to flame break out is small, consistent with a “gravitationally confined detonation” occurring at a later epoch, but additional burning will occur following breakout that may modify this conclusion.

Subject headings: supernovae: general — white dwarfs — hydrodynamics — nuclear reactions, nucleosynthesis, abundances — convection — methods: numerical

¹Department of Astronomy & Astrophysics, The University of California, Santa Cruz, Santa Cruz, CA 95064

²Center for Computational Sciences and Engineering, Lawrence Berkeley National Laboratory, Berkeley, CA 94720

³Department of Physics & Astronomy, Stony Brook University, Stony Brook, NY 11794

1. Introduction

It is generally agreed that a Type Ia supernova (SN Ia) is the thermonuclear explosion of a carbon-oxygen white dwarf driven to instability by the accretion of mass from a binary companion, but the nature of the progenitor star and just how the burning ignites and spreads is debated (e.g. Hillebrandt & Niemeyer 2000; Hillebrandt et al. 2013). Here we focus on the “single degenerate, Chandrasekhar mass” (MCh) model where the white dwarf accretes material from its binary companion slowly enough to reach $1.39 M_{\odot}$ and ignite a subsonic carbon runaway near its center. As the temperature rises in response to the burning, the white dwarf expands very little because the matter is degenerate. A growing convection zone develops, however, and carries the excess energy from the center outwards where it gradually heats an increasing fraction of the white dwarf to high, but not explosively high temperature (Baraffe et al. 2004). After about a century of this simmering (Woosley et al. 2004), the central energy generation rate exceeds what can be carried away by convection and the burning becomes increasingly localized. The temperature gradient steepens rapidly, reflecting the high power upon which the carbon fusion rate depends. Eventually a discontinuity develops between fuel and ash and a “flame”, or “deflagration” is born.

Extensive literature exists regarding the subsequent propagation of these flames, once ignited, but the geometry assumed by various authors for that ignition varies greatly. Some assume ignition at a single point at, or very near the center (Khokhlov 1995; Niemeyer et al. 1996; Gamezo et al. 2005; Townsley et al. 2007; Jackson et al. 2010; Krueger et al. 2012; Ma et al. 2013); others employ many ignition kernels distributed throughout an extended region of the stellar interior (García-Senz & Bravo 2005; Röpke & Hillebrandt 2005; Röpke et al. 2006, 2007a; Kromer et al. 2013). It is generally agreed, however, that in the absence of detonation, the ensuing deflagration by itself produces too little ^{56}Ni and ejects matter that is too well-mixed when compared to the stratified ejecta observed in typical SN Ia spectra (although see Kromer et al. (2013) for a recent pure deflagration model applied to a class of sub-luminous SNe Ia). Simulations that successfully match supernova observations therefore usually insert, by hand, a transition to detonation once the deflagration has reached some threshold condition. This “deflagration-to-detonation transition” (DDT) (Khokhlov 1991) produces an ejecta velocity structure with sufficient intermediate mass elements (IME) and iron-group elements (IGE) to reasonably match observations of typical SN Ia.

Since the detonation always follows a deflagration that sets the initial conditions, the final SN Ia model is sensitive to how the subsonic burning is modeled and, as we shall see, to exactly how it is ignited. The simplest assumption would be to ignite the runaway at the dead center, but this overlooks the fact that matter there is not at rest. As the matter moves around, it carries within it the “sparks” that can potentially develop into an explosion. The

idea that the convective flow would naturally lead to off-center ignition was first explored by Garcia-Senz & Woosley (1995) who estimated a displacement from the center of several hundred km. Höflich & Stein (2002) modeled a two-dimensional wedge of the white dwarf with the center cut out, and found inwardly moving convective plumes caused compressional heating that triggered a runaway in a single downward moving hot spot very near the center. Three-dimensional simulations using an anelastic hydrodynamics code (Kuhlen et al. 2006) painted a somewhat different picture however, finding an overall dipolar nature for the convective flow and ignition in an *outwards* bound flow, again about 100 km off center. This was consistent with analytic estimates (Woosley et al. 2004; Wunsch & Woosley 2004), but was somewhat sensitive to the need to prescribe an artificial “hole” in the center of the anelastic hydro grid (which used spectral coordinates), and thus questionable.

More recently, full star simulations have been performed (Zingale et al. 2009; Zingale et al. 2011; Nonaka et al. 2012, hereafter, N12) of the last few hours of convection using the low Mach number stellar code Maestro (Nonaka et al. 2010) and a Cartesian grid with adaptive mesh refinement (AMR). These calculations, done so far only for non-rotating or slowly rotating white dwarfs, clearly show ignition only happening a single time and in a very small region. The most likely off-center displacement for the ignition lies in a range 40 to 75 km, with a small probability extending inwards to the origin and outwards to 110 km. That is, the final runaway, while always starting at a single point, is chaotic in its location. There is not a single prescribed radius, but a range of possibilities depending on random flows just prior to runaway. The distinction between central ignition and ignition even slightly off center is dramatic. Once the star begins to burn on one side, it never burns, as a deflagration, in the inner regions of the other side. The resulting supernova is inherently asymmetric.

In this paper, we use the compressible hydrodynamics code, Castro (Almgren et al. 2010b), to follow the evolution from the time the first point runs away up to break out of the deflagration through the surface of the star. While only part of a full explosion model, this is a sufficiently complex problem to justify its own careful analysis. It is also an important step in our ultimate goal, a full, end-to-end treatment of the explosion of Chandrasekhar mass white dwarfs, from convection through homologous coasting as supernovae. In this paper, however, we do not include any deflagration-to-detonation transition and do not calculate ejecta composition or light curves.

Since the Maestro and Castro codes both use the same BoxLib software framework (Bell 2013; Rendleman et al. 2000; Almgren et al. 2010a), it is straightforward to import the turbulent ignition conditions directly from the convection simulation into Castro, while retaining the same initial grid structure and data. Previous work of this sort was done

in two dimensions with an artificial velocity field (Livne et al. 2005). Here we investigate the role of a realistic, three-dimensional background convective flow field on the flame as it rises and expands towards the stellar surface. We also compare our results to analytic models developed for burning thermals on small scales in the presence of turbulence and gravitational stratification from Aspden et al. (2011).

An additional advantage of the new study is the very fine spatial resolution employed. This is accomplished by using several levels of AMR and made feasible by early access to the NSF Blue Waters machine. Although still many orders of magnitude too coarse to resolve the flame thickness, the resolution used here is fine enough that the initial laminar propagation of the flame is well resolved before it begins to float and become highly turbulent. During this laminar phase, existing perturbations burn out and the ash exists for a time as an almost perfectly spherical bubble. This is important because, as we shall see, the outcome is quite sensitive not only to the location of the ignition point, but how perturbations of the flame surface evolve.

2. Numerical Setup

For our study, we used the compressible multi-dimensional hydrodynamics code Castro (Almgren et al. 2010b). This code has been optimized to scale well on upwards of 100,000 processors (Almgren et al. 2010a) and is capable of employing multiple levels of AMR with subcycling in time. As initial input, the 4.34 km zone⁻¹ model (hereafter the N12 model) of Nonaka et al. (2012) was employed. This model of a Chandrasekhar mass white dwarf, calculated using the Maestro code, ignited a runaway at a representative radius of 41.3 km. The Maestro simulation used two levels of AMR with a finest resolution of 4.34 km (effectively 1152³ zones) and that is the same zoning used in the initial remap into Castro. The Maestro data is employed for the entire star, including the turbulent velocity field, temperature, density, and pressure. The equation of state is the same but the treatment of nuclear burning differs. Maestro used a simple reaction network adequate only for carbon burning. The present study uses tables evaluated using a much larger network (see Section 2.2). For simplicity, the composition of the N12 model was reset everywhere to be a 50-50 mixture of ¹²C and ¹⁶O. This is a reasonable approximation since the burning during the simmering phase of the N12 simulation only decreased the carbon/oxygen mass fractions from 0.5 to 0.49.

The link time, when the transition was made from Maestro to Castro, was when the temperature in any zone in the N12 simulation first exceeded 8×10^8 K. Other nearby zones were too cool to run away in the same time frame. As discussed in Nonaka et al. (2012), this

transition time was 0.57 s earlier than the time when the actual runaway occurred, as defined by the first production of iron-group nuclei and the formation of a flame at $T \sim 1.1 \times 10^9$ K. Following the evolution with Maestro beyond this point would have violated the time step limits in the code (burning time shorter than the time for a fluid element to cross the zone) and that was when the data dump was made. Continued evolution with this criterion relaxed showed that the hot spot moved less than two zones before flashing to very high temperature. We do not think this 0.57 s (one to two zone) offset affects our results in any important way.

2.1. Castro Initialization from Maestro Data

Although they share the same underlying data structures, Maestro and Castro solve fundamentally different hydrodynamic equations. Unique to Maestro is the concept of a one-dimensional, radial *base state* of density, ρ_0 , and pressure, p_0 , that are in hydrostatic equilibrium and represent the “average” state as a function of radius (see Nonaka et al. 2010 for details). Using low Mach number asymptotics, the pressure is decomposed into a base state pressure and a perturbational pressure, $p(\mathbf{x}, t) = p_0(r, t) + \pi(\mathbf{x}, t)$, where the base state pressure is used in place of the full state pressure everywhere except in the momentum equation. This replacement effectively allows the base state pressure to govern the thermodynamics of the fluid while the dynamics are driven by the perturbational pressure. Next, the equation of state is recast as a divergence constraint on the velocity field. Using this model, sound waves are filtered from the system, thus allowing for larger time steps under the *advective*, rather than acoustic, Courant condition.

When transforming the low Mach number results to a fully compressible code, one has several options for determining the thermodynamic state of the fluid (Nonaka et al. 2011). For example, the pressure field in the compressible data set could be set equal to p_0 , $p_0 + \pi$, or determined from the equation of state (EOS) given the composition, temperature, and density from the Maestro data set. Therefore, although the various methods of mapping from the Maestro code to the Castro code may be analytically equivalent (to $\mathcal{O}(M^2)$), there are inherent numerical differences that may lead to thermodynamic inconsistencies. Also, one must take care when interpolating data from the one-dimensional, radial base state to the three-dimensional Cartesian grid used to hold the full state quantities. The approach we took, which minimizes the development of spurious pressure waves from hot spots at the beginning of the Castro simulation, is as follows:

1. Extract the velocity, density, base state and dynamical pressure from the Maestro simulation at the time of ignition.

2. Reset the composition to a 50 - 50 mixture of ^{12}C and ^{16}O .
3. Use quadratic interpolation of the radial base state pressure and add the Cartesian grid-based dynamical pressure to formulate the full pressure field on the Cartesian grid.
4. Use the pressure, density, and composition as input to the EOS to obtain the temperature and internal energy fields.

We note that resetting the initial composition from the N12 model’s values effectively decreases the mean molecular weight in regions where significant carbon burning was present in the N12 simulation. This decrease in molecular weight corresponds to a decrease in temperature of less than 5% in those regions. The thermal gradient is much more sensitive to the pressure and density than the composition, and therefore the thermal gradient is left essentially unchanged with our resetting of the composition. Regions that were convectively unstable in the N12 simulation remain unstable in the simulations presented here; however, we do not capture the central carbon burning that is driving the convection. In addition, the resetting of the composition alters the ^{22}Ne content of the N12 ash state, but this is likely to have little affect on the deflagration evolution (Townesley et al. 2009).

In addition, care must be taken when importing data near the edge of the star. To prevent large velocities from developing in Maestro below a specified low density cutoff, $\rho_c = 10^6 \text{ g cm}^{-3}$, the algorithm changes its velocity divergence constraint to behave more like that of an anelastic approximation. Also, once the density has fallen below $\rho = 10^5 \text{ g cm}^{-3}$, both ρ_0 and p_0 are held constant (see Nonaka et al. 2010 for details). Castro can handle densities much lower than the typical cutoff density used in Maestro. We therefore overwrote the Maestro data at the edge of the star to drop the density down to a much smaller value than the Maestro cutoff density. The first step is to examine the radial base state density from Maestro, ρ_0 . We find the radial coordinate, r_c , where the density drops below ρ_c , and we use the base state density and temperature in a 50 - 50 mix of ^{12}C and ^{16}O to create a one-dimensional model in hydrostatic equilibrium (HSE) outward from r_c , following the procedure of Zingale et al. (2002). The one-dimensional model is then interpolated onto the full Cartesian grid, overwriting the Maestro data for zones with $r \geq r_c$. Figure 1 shows the average radial profiles of both density (black) and temperature (red; right axis) for the N12 model (solid) and our mapping of this model into Castro (dashed). The vertical dotted line marks the location where the density fell below $\rho_c = 10^6 \text{ g cm}^{-3}$ in the N12 model, and we reconstruct the HSE model.

2.2. Microphysics

The N12 model used as input and the simulations presented in this paper both use the Helmholtz EOS of Timmes & Swesty (2000), which includes contributions from relativistic and non-relativistic electrons of arbitrary degeneracy, ideal ions, radiation, and Coulomb corrections. Thermal diffusion was not present in the simulations of N12, but is included here in order to move the flame (see Section 2.2.1).

The treatment of nuclear reactions differs substantially between those used to calculate the N12 model and this paper and warrants explanation. The N12 model used a very sparse reaction network described in Zingale et al. (2011), which was based upon the work of Chamulak et al. (2008). This network included only the $^{12}\text{C}+^{12}\text{C}$ heavy ion reaction and a multiplier to account for the energy release of subsequent reactions. The “ash” composition of this artificial reaction was a mixture of ^{13}C , ^{16}O , ^{20}Ne , and ^{23}Na with an average atomic weight and charge of $A_{\text{ash}} = 18$ and $Z_{\text{ash}} = 8.8$.

Here, depending upon the density, burning may proceed through carbon, neon, oxygen, and silicon burning, all the way to nuclear statistical equilibrium (NSE). The “ash” can continue to evolve via electron capture, alpha capture, and photodisintegration reactions even after the burning front has passed. The necessary nuclear physics is therefore more complex. To make this problem tractable in three dimensions, the tables described in Ma et al. (2013) were employed. To briefly review, the nuclear burning is divided into two phases: reactions inside the flame and reactions after the flame has passed. Inside the flame, burning is assumed to occur at constant pressure, with results that are most sensitive to the density and electron fraction, Y_e , of the degenerate gas and very little to the initial temperature. The initial density and composition of the fuel thus determine the energy yield and final composition which are computed off-line using a large reaction network containing 188 isotopes up to $A = 72$. To save space these abundances are packed into just seven abundance variables: “helium” (for $A < 12$), “carbon” ($12 \leq A < 16$), “oxygen” ($16 \leq A < 20$), “neon” ($20 \leq A < 24$), “magnesium” ($24 \leq A < 28$), “silicon” ($28 \leq A < 48$, IME), and “iron” ($A > 47$, IGE). This treatment of the burning is applied when the temperature rises by conduction to above 2×10^9 K in zones with a density above 3×10^6 g cm $^{-3}$ and a carbon mass fraction over 1%.

After the flame has passed, energy can still be generated or absorbed by further evolution of the NSE ashes of the flame. This proceeds by a combination of photodisintegration, recombination, β -decay, positron decay and e -capture reactions, which depend on the temperature, density, and Y_e of the NSE ashes. For this phase a separate table was constructed offline using a NSE network with 127 isotopes up to $A = 60$. The changes from the NSE evolution are interpolated from the table and then packed into the helium, silicon, and iron

groups of our abundance variables. The table was called for “ash” zones defined by high temperature, the presence of iron, and the absence of carbon. In particular the NSE tables were used when the temperature was above 3×10^9 K, density above $\sim 10^8$ g cm $^{-3}$, and the combined helium and iron group abundance above 88%. The cutoff in helium plus iron abundance was determined empirically to assure that the NSE table was only called on zones that were actually in NSE, even at very high temperature where silicon and calcium can exist in abundance..

2.2.1. Thickened Flame Model

For the conditions characterizing ignition inside a nearly Chandrasekhar mass white dwarf, the thickness of the laminar thermonuclear flame is less than a millimeter (Timmes & Woosley 1992). Turbulence and other instabilities twist and churn this thin flame sheet into a complex topology that increases the area and the effective burning rate. Resolving these structures while simulating large fractions of the star in three dimensions is not computationally feasible. In the astrophysical and chemical combustion communities, such “turbulent flames” are usually handled in one of two ways: 1) by spreading the flame over several grid zones, creating a *thickened flame* whose propagation is determined by advection, the energy release from burning, and thermal diffusion across the flame front (e.g. Khokhlov 1995), or 2) by treating the flame as a discontinuity, using *level sets* to identify the flame surface, and solving advection equations to propagate the flame (e.g. Reinecke et al. 1999). Both methods have their strengths. For simplicity, we follow here the work of Ma et al. (2013) and use the thickened flame model described therein. Here we briefly review the basic principles.

In a thickened flame model, the combustion region is usually identified by a *progress variable*, which characterizes the degree of completion of the burning (e.g. Khokhlov 1995; Townsley et al. 2007). In our model, the progress variable is the carbon mass fraction which ranges from fuel ($X(^{12}\text{C}) = 0.5$) to ash ($X(^{12}\text{C}) \lesssim 0.01$). The thickened flame is artificially spread over a number of computational zones, n , such that the flame thickness, $\delta = n\Delta x$, can be resolved on a grid with spacing Δx . By specifying both n and the flame speed, v_f , a time scale is determined, $\tau = \delta/v_f$, that allows the calculation of an effective “opacity”

$$\kappa = \frac{c\tau}{3\rho(n\Delta x)^2}, \quad (1)$$

and coefficient of thermal conduction,

$$K = \frac{4acT^3}{3\rho\kappa} = 4aT^3 \frac{(n\Delta x)^2}{\tau}, \quad (2)$$

where c is the speed of light and a , the radiation constant. The energy generation rate is then given simply by the need to burn up the carbon in the defined region on the specified time scale,

$$\epsilon_{\text{nuc}} = 9.64 \times 10^{23} \frac{d[BE/A]}{d[X(^{12}\text{C})]} \frac{d[X(^{12}\text{C})]}{dt} \text{ erg g}^{-1} \text{ s}^{-1}, \quad (3)$$

where $d[BE/A]/d[X(^{12}\text{C})] \simeq \Delta(BE/A)/0.5$, and $\Delta(BE/A)$ is the total change in nuclear binding energy (in MeV) per nucleon when carbon fuel burns to ash at the given density and ^{12}C mass fraction. This quantity is determined from interpolation in a table. The rate of change of carbon abundance in the flame is then $d[X(^{12}\text{C})]/dt \simeq -0.5/\tau$. For dense regions with very little residual carbon ($X(^{12}\text{C}) \lesssim 0.02$), this prescription gives too slow a decrease, so the remaining trace of carbon is burned more quickly by using $d[X(^{12}\text{C})]/dt \simeq -X(^{12}\text{C})/\Delta t$, with Δt the time step. Given some desired flame speed and thickness, the local density and the nuclear yield table thus determine a self-consistent thermal diffusion coefficient and energy generation rate that move the flame front accordingly. In practice, n varied between three and eight.

It remains to choose the effective speed of the flame. While the laminar speed sets a lower bound, there are other important factors. The buoyant growth of Rayleigh-Taylor modes or local shear and turbulence can wrinkle or stretch the flame front, increasing the overall surface area for heat transport resulting in an increased burning rate. There are several ways this enhancement has been treated in past supernova models (see Ma et al. 2013, for a discussion). The speed could be chosen as to burn out any sub-grid structure assuming the dominance of the Rayleigh-Taylor instability in creating that structure (Khokhlov 1995; Zhang et al. 2007), i.e. $v_{\text{eff}} \approx F(g_{\text{eff}}\Delta x)^{1/2}$ with g_{eff} the acceleration due to gravity times the Atwood number ($\sim 10^9 \text{ cm s}^{-2}$), Δx , the grid scale (typically 10^5 to 10^6 cm), and F , a constant less than 1. This gives flame speeds $\sim 100 \text{ km s}^{-1}$. Or, perhaps more physically, one could analyze the turbulent flows on the grid in the vicinity of the flame and obtain a representative turbulent speed at the grid scale (e.g. Schmidt et al. 2006a,b). Röpke (2007) finds values for v_{eff} that vary with location, but whose distribution peaks, again, typically at 100 km s^{-1} , but with an extended tail well past 200 km s^{-1} . This approach, however, requires additional coding that has not yet been implemented and tested in Castro. In Ma et al. (2013), a constant value was assumed for v_{eff} , and it was found that the answer for turbulent deflagration in the interior of the white dwarf was insensitive to the value chosen for v_{eff} in the range 50 to 200 km s^{-1} . Furthermore, Model BT of Ma et al. (2013) used a simplified model turbulent flame speed constructed from the local grid-scale turbulent intensity and found that the resulting nucleosynthesis and bulk flame properties depended more upon the initial conditions than on the choice of a fixed or turbulence-based variable flame speed.

Here we continue to follow the constant flame speed procedure of Ma et al. (2013). The flame speed is set to a constant value, $v_f = \max(50 \text{ km s}^{-1}, v_l)$, where v_l is the laminar flame speed as determined in Timmes & Woosley (1992). This speed is consistent with the A50 simulations of central ignition from Ma et al. (2013), but is a bit slower than typical turbulent speeds ($\sim 100 \text{ km s}^{-1}$). The smaller value was used in order to retain additional structure on our very fine grid and avoid undue “fire polishing”. In our next paper, we will explore a more realistic flame speed distribution based upon a sub-grid turbulence model. In the Appendix to this paper we have included a few test problems that ensure the flame is moving as expected under various velocity-field conditions. As discussed later in the paper, both the Rayleigh-Taylor based model and the constant flame speed model may become highly suspect once the burning breaks out and starts to spread over the surface of the white dwarf.

3. Simulations

Our simulations begin with output from the N12 model calculated using the Maestro code at $t = 10562.5$ seconds, corresponding to the time where the temperature first exceeds $8 \times 10^8 \text{ K}$ in a single ignition zone. The coordinate system has the center of the star as its origin so the hottest point in the domain is located $r = 41.34 \text{ km}$ off-center. Two main runs are carried out (hereafter the A series) that use this point as the ignition location, one with the background convective flow field (Model AV) and one with the initial velocity field set to zero (Model A0). Four similar calculations were also carried out with the ignition point arbitrarily moved to 10 km off-center (Models BV and B0) and to the center of the star (Models CV, C0). The A series of models was evolved the longest ($\sim 0.8 \text{ s}$) while the series B and C simulations were only used to investigate differences in the early evolution. For computational efficiency, all simulations calculated gravity using a monopole approximation as described in (Almgren et al. 2010b). Table 1 summarizes the properties of the various models.

The N12 output file from Maestro had one level of refinement (i.e., a total of two levels), with its finest level having a resolution of $4.34 \text{ km zone}^{-1}$ in all regions with $\rho > 5 \times 10^7 \text{ g cm}^{-3}$. In the present study, the single ignition zone of N12 is replaced by a highly resolved spherical bubble with an average radius of $\sim 2 \text{ km}$, but with a perturbed surface. In order to have the necessary ~ 10 's of zones to resolve the bubble surface, additional refinement well beyond that in the Maestro initial model was necessary. In addition, our thickened flame model (Section 2.2.1) spreads the flame over several zones such that a higher resolution corresponds to a more realistic (albeit still under-resolved) flame. This particular flame

model has been used at much coarser resolution (Ma et al. 2013; Dong et al. 2013), and the general evolution and features of the burning model do not depend sensitively on the resolution used with the caveat of the initial laminar burning phase discussed below discussed in Section 4.1. We note that this laminar stage is very quickly burned through within a few time steps (likely even unnoticed) in simulations with coarser resolution, such as in Dong et al. (2013), for example, where the ignition spot was much larger ($r = 20$ km, compared to our ~ 2 km), but with perturbations of the same relative size.

The addition of levels of refinement began by first mapping the N12 data into the Castro framework, as described in Section 2.1, onto a *fixed* grid structure that was exactly the same as in the N12 simulation (refer to Figure 2). The system was then evolved for ten coarse-level time steps (0.5 ms) to adjust to the new framework. Next, the system was evolved for an additional ten coarse-level time steps (1.3 ms), while allowing the grids to change based on the same AMR refinement criteria as before (we note that Castro uses tighter grid generation tolerances, so that the Castro grid structure is slightly different).

Additional levels of refinement were then added one at a time, with ten coarse-level time steps between each addition. To reach our target resolution of ~ 135 m zone $^{-1}$, we used levels with varying refinement ratios — the jump in resolution when going from a coarse grid to the next finer grid. A total of five levels was finally employed with refinement ratios of either two or four, giving the resolution as 8.68, 4.34, 1.09 km zone $^{-1}$, 271.3, and 135.6 m zone $^{-1}$ for each level from coarsest (level 0) to finest (level 4). The initial refinement criteria for selecting the zones to be refined to a specific level was based on the density. Zones were placed in level l if their density is greater than ρ_l , with $\rho_1 = 5 \times 10^7$, $\rho_2 = 1.5 \times 10^9$, $\rho_3 = 2.49 \times 10^9$, and $\rho_4 = 2.5 \times 10^9$ g cm $^{-3}$. These particular values of ρ_l were carefully chosen along with the number and size of grids that get blocked together on a single MPI task to ensure efficient computational load balancing.

After all the levels of refinement had been added, the system was evolved for an additional 50 coarse-level time steps in Castro to guarantee relation to the new grid. The CFL condition for the size of the time step is different between Maestro and Castro. In particular, the low Mach number approximation in Maestro allows a stable time step using an advective CFL condition rather than an acoustic CFL condition, so that the Maestro time step is *at least* a factor of $1/M$ greater than the allowable time step in Castro, where M is the maximum Mach number in the simulation. At the time of ignition, the Maestro time step is a factor of 18 greater than the maximum allowable Castro time step. Furthermore, we limit the initial time step size in Castro to be a factor of 0.05 times the allowable time step and allow it to grow by no more than 10% per time step. This implies that even though the system has been evolved for 50 Castro time steps before we have reached our final grid

resolution, the total elapsed time (0.017 s) is less than a single Maestro time step, and the conditions on the grid have not changed appreciably.

It is important to note that adding levels of refinement alters the turbulent structure of the high Reynolds number velocity field. In particular, increasing the resolution increases the simulation’s inertial subrange of the energy cascade in wavenumber space (see Figure 20(c) of N12, for example). Once a level is added, the small-scale eddies present before the addition can break down to smaller scales. There is a time scale associated with the traversal of an eddy through the inertial range. In high Reynolds number flow, large-scale eddies (size L) take approximately an eddy turnover time (t_L) to break down to the Kolmogorov dissipation scale. Smaller eddies have smaller turnover times ($t_l/t_L \sim (l/L)^{2/3}$), and they breakdown to the dissipation scale in less than an eddy turnover time. The cascade of turbulence to “fill in” the added level in our simulations should happen quicker than the typical small-scale eddy turnover time from N12 ($\lesssim 0.1$ s). That said, AMR levels were added on a shorter timescale — the turbulent energy in our simulations may not have had sufficient time to completely cascade to the smallest scales. A further resolution study is required to determine the degree of incomplete energy cascade. We note, however, that the turbulent velocities on the 4 km-scale in N12 were of order 14 km s^{-1} , much less than the laminar flame speed ($\sim 100 \text{ km s}^{-1}$). The turbulent fluctuations on our finest grid (a factor of 32 more refined than N12) should then be even smaller due to Kolmogorov scaling arguments ($u_l/u_L \sim (l/L)^{1/3}$).

For the A series simulations, the location of the ignition point was determined by the hottest grid zone in the initial Maestro data; for the B(C) series, the ignition point was artificially placed at $x = y = 0$ and $z = 10(0)$ km. The ignition point for series A was naturally in a region of outflow with radial velocity $\sim 10 \text{ km s}^{-1}$ (see N12). The artificially placed ignition point for series B was also in a region of outward radial velocity, however there was a non-negligible ($\sim 30\%$) azimuthal velocity contribution to the local velocity, the total speed of which was approximately $\sim 40 \text{ km s}^{-1}$. The ignition spot was defined as a sphere of ash having radius 2 km perturbed by random spherical harmonics. The thermodynamic state was set by the properties of ashes from nuclear burning as given by the table described in Section 2.2 with temperature $T = 8.5 \times 10^9$ K, average binding energy per nucleon $BE/A = 8.166$ MeV, and average atomic mass $\bar{A} = 11.6$. The density of the ash is determined cell-by-cell from the isobaric burning condition and the EOS; typical values are around $\rho \sim 2.15 \times 10^9 \text{ g cm}^{-3}$. The ^{12}C mass fraction jumps from 0.5 in the fuel to $\sim 10^{-5}$ in the ash. We use the ^{12}C mass fraction and its gradient as refinement criteria for AMR to better restrict our finest level coverage to the ash and its surrounding region. Figure 2 shows the progression of adding levels from the initial N12 grid structure (top left) through the inclusion of our hot spot, shown as a blue contour of $X(^{12}\text{C}) = 0.49$ (lower right).

For comparison to other simulations in the literature, we consider the fully refined grid with added ignition point as our initial conditions for the simulations presented here. That is, any evolution of the system during the addition of levels of refinement is ignored, and $t = 0$ s once the ignition spot is in place.

The simulations presented here used the resources of several supercomputing facilities. Most of the calculations were done using the Early Science System of the Blue Waters supercomputer at NCSA. While this machine was closed for upgrades to the full Blue Waters machine, which was also used in later simulations, the calculations were continued on the Titan machine at OLCF and on the Hopper supercomputer at NERSC. It should be noted that although the performance of the pre-production Blue Waters systems did not represent the full scalability of the complete machine, the validity and integrity of the data and calculations performed therein have been verified to be sufficiently consistent with those on other full-production machines. The calculations were run on a maximum of 65,536 cores (4096 MPI tasks, each with 16 OMP threads). For computational efficiency, the finest level of refinement was derefined once it contained $\sim 1.1 \times 10^9$ zones. For example, in the A series of runs this happened at 0.4 s and again at 0.59 s. The maximum number of grid zones at any given time was just over 2×10^9 . The two A series runs used approximately 20 million CPU hours each; the B and C series of simulations together used approximately 30 million CPU hours.

4. Results

4.1. Series A: Natural Ignition Location

The most direct mapping from the N12 simulations is Model AV. The left panel of Figure 3 shows the initial flame surface of Model AV as denoted by an isocontour of $X(^{12}\text{C}) = 0.45$. The initial hot spot has a diameter of ~ 4 km plus random perturbations on the scale of a few hundred meters. The middle ($t = 0.0059$ s) and right ($t = 0.0119$ s) panels of Figure 3 show the evolution of the flame surface as it quickly burns through the initial perturbations. At the ambient density of the flame’s initial location, the laminar flame speed is about 95 km s^{-1} (Timmes & Woosley 1992), which is greater than the constant (lower bound) speed we assumed, and therefore the flame initially burns laminarily. Since the density is nearly constant in the small region involved, the bubble remains nearly spherical and increases in volume by $\sim 80\%$ during the first ten milliseconds of evolution, although there is less expansion on the bottom of the bubble where the burning has to directly compete with buoyancy. Indeed, the perturbations on the underside of the bubble are not completely burned out this early in the evolution. The bubble does not experience significant buoyant

rise for another twenty milliseconds, however, after which its volume has increased another order of magnitude. An initial ignition point of ~ 5 km in radius with smaller relative perturbations would probably yield a similar starting point (see Section 4.4.1).

Figure 4 shows the same isocontour as in Figure 3, but at later times. The persistence of perturbations on the underside is seen in the left panel ($t = 0.15$ s) of Figure 4. Around $t = 0.26$ s (middle panel), instabilities start to wrinkle the flame’s surface. By this time, the cap of the bubble has also rolled up into itself creating a more traditional “mushroom” shape. By $t = 0.47$ s (right panel), the outer edge of the bubble is a little more than half way through the star’s convective region, and the volume enclosed by its highly wrinkled surface is $\sim 1.5 \times 10^5$ times the original hot spot’s volume.

Figure 5 shows volume renderings of the magnitude of vorticity at the same time and spatial scales as used in Figure 4. Large values of vorticity are shown as the yellow-white tubes and indicate regions of high turbulence. Early in the evolution, the vorticity is confined to a single torus similar to the behavior found in previous simulations (Aspden et al. 2011). In this stage, the cap of the buoyant bubble is forming as fresh fuel is being entrained from the edges and rolled under the brim of flame’s surface. Later, the vortex tube bundle comprising the single dominant torus begins to break apart and spawns smaller vortex tubes that flow along the bubble’s surface. Eventually there are several vortex tubes lying on the flame’s surface and they dominate over the now nearly destroyed torus-shaped bundle of vortex tubes making the brim of the bubble, as seen in the middle panel of Figure 5. At even later time shown in the right panel, the strong turbulence has warped high vorticity tubes into the interior of the bubble as well as the trailing tail of the plume.

Model A0 was similar to Model AV. Figures 6, 7, and 8 show a comparison as slices of various quantities at $t = 0.5$ s, $t = 0.6$ s, and $t = 0.75$ s, respectively, for Model AV (top two rows) and Model A0 (bottom two rows). The plots in each column are, from left to right: temperature, magnitude of vorticity, and energy generation rate. For all three figures (6,7, and 8), the color range for temperature varies smoothly and linearly between blue (10^9 K) and the maximum temperature in the slice, which was several billion Kelvin. Also in these figures, the color range for vorticity is logarithmically spaced between 100 s^{-1} (blue) and the maximum (white) value in each slice, which, as in the volume renderings of Figure 5, was several thousand s^{-1} . The energy generation rate color maps are divided between endoergic reactions (blue) and exoergic reactions (red); only values within 0.1% of each extrema are colored. The thin, horizontal white lines across the top row for each model show the location of the orthogonal slice depicted in the bottom row; the slice location was chosen to be through the region of largest lateral extent. The top panels have an aspect ratio shown with distance indicators, whereas the bottom panels have a one-to-one aspect

ratio using the horizontal scale indicated.

At $t = 0.5$ s in Figure 6, the bulk of the high vorticity lies just interior of the outer edges of the flame, although some turbulence is deeper within the ash, for both Models AV and A0. There are pockets of high temperature and exoergic reactions, but also pockets where cold, fresh fuel has been entrained under the roiling lip of the flame. Some of these pockets are on the order of 50 km in size, but do not last very long as turbulence quickly pulls them apart into ever smaller regions that can burn quickly as heat diffuses through their surface. Reactions within the flame itself are always very exoergic and most of the energy from nuclear burning is released there, as indicated by the solid red tracing the flame’s outline in all energy generation rate (right) panels. There is a small amount of photodisintegration (blue) just interior to the outer flame surface. Interior to this endoergic reaction region, the exoergic reactions become much more prominent as expansion and cooling lead to reassembly of alpha particles to iron. Both Models AV and A0 have a similar shape and structure, but the vertical extent of Model A0 is slightly less owing to the lack of an initial outward velocity field present in Model AV. Furthermore, the stem and cap of the bubble of Model A0 tend to be more slender than the equivalent features of Model AV. In both cases, the aspect ratio of the bubble’s shape is nearly 1 : 2.

In Figure 7 ($t = 0.6$ s), regions of high vorticity are again largely confined interior to the flame’s surface. Endoergic reactions are now nearly exclusively found just behind the periphery of the flame with very little in the interior, even in the vicinity of pockets of fresh fuel. This shift in burning behavior occurs as the bubble reaches lower density where the cross sections for endoergic reactions drop appreciably and NSE processing is stunted. Also at lower density and larger extent, the bubble more easily expands laterally due to lateral pressure gradients (see Section 4.4), leading to an accelerated increase in the bubble’s aspect ratio to nearly 2 : 3. At this time the cap of the bubble is nearly isothermal at $\sim 3 \times 10^9$ K for both models. Again, we notice that the features of Model A0 tend to be narrower than those of Model AV, however the disparity appears to be decreasing. The bubbles are just about to cross the original location of the convective boundary.

Figure 8 ($t = 0.75$ s) also shows the $\rho = 10^8$ g cm⁻³ (interior) and $\rho = 10^7$ g cm⁻³ (exterior) isocontours as dashed grey lines; the $\rho = 10^6$ g cm⁻³ contour lies just outside the edge of the image and is slightly puffed out due to the expansion caused by the bubble. One feature that is immediately noticeable is that below $\rho = 10^8$ g cm⁻³, there is very little energy generation; indeed, only exoergic reactions occur below this density (see Section 2.2), and only in the vicinity of fresh fuel. The caps of the bubbles are no longer nearly isothermal, but have a temperature gradient that goes from $\sim 2.4 \times 10^9$ K in the center to just over 10^9 K near the perimeter. Both Models A0 and AV have the bulk of their high vorticity regions

again on the periphery of the ash, and there is a decrease in vorticity in regions absent of strong reactions. The disparity in the features of the two models has diminished. Both models have reached about the same radial extent, ~ 1700 km, and have assumed a nearly 1 : 1 aspect ratio due to significant lateral expansion.

One source of the vorticity generated in Figures 6, 7, and 8 is due to the baroclinicity, ψ :

$$\vec{\psi} = \frac{1}{\rho^2} \nabla p \times \nabla \rho. \quad (4)$$

The burning within the flame front itself is isobaric, but a density gradient forms as cold fuel is burned to hot ash. This causes a misalignment of the local pressure and density gradients and thus a nonzero baroclinicity, which generates vorticity. Figure 9 shows an example of the magnitude of baroclinicity for Model AV at $t = 0.8$ s. The colorbar goes from ψ less than 1 (white) to 3.3×10^6 s $^{-2}$ (black). It is interesting that the strongest baroclinicity occurs within the tail of the flame and along the underside of the cap of the bubble. However, in the tail, $\vec{\psi}$ is orthogonal to the flame surface, whereas the cap has $\vec{\psi}$ nearly parallel to its surface. In the tail, this alignment creates flow mainly along the direction of the plume. The vorticity generated near the cap tends to entrain fresh fuel across the flame surface. Fuel is still entrained into the tail of the flame, but not nearly as vigorously as in the cap.

In addition to the minor morphological differences between Models AV and A0, there are also small differences in the nucleosynthetic yields. Figure 10 shows the evolution of the production of iron-group (top panel) and IME (bottom panel) elements for both Model AV (blue) and Model A0 (red). The thin, dashed, grey line is the percent difference between the two models. In general, Model A0 burns more material than Model AV, likely owing to the lack of an initial push from the outward plume present in the N12 data. However, given the stated assumptions of our thickened flame model, the background turbulence affects the nucleosynthetic yields on the 10% level for an ignition point placed at the runaway location indicated by our low Mach number calculations. It is important to note that this is only the affect during the evolutionary period when the bubble is buoyantly rising towards the surface. Any subsequent burning after the flame has broken through the white dwarf’s surface (e.g DDT) can either increase or decrease the final yield difference depending on the details of the local density and composition. The convective flow field in the interior likely has a negligible effect on the post-breakout burning. Table 1 lists the latest time evolved for these models, t_{\max} , including the farthest distance reached by the burning, r_{\max} , and the total amount of IME, IGE, and nuclear energy release produced at the end of the simulations. The total amount of material burned during the deflagration depends quite sensitively on the initial conditions (i.e. location and size — or solid angle) of the ignition point; this is being explored with our flame model in an upcoming paper (Dong et al. 2013). We note that the nuclear

energy released in our A series of simulations is comparable to that of the deflagration phase of Models 16b100o8r, 25b100o6r, and 25b100o8r of Jordan et al. (2008). Also, for the A series of simulations, t_{\max} is approximately equal to the time the flame first hits the $\rho = 10^7$ g cm⁻³ surface; at this point, the central density was $\rho_c = 2.27 \times 10^9$ g cm⁻³.

While it is of paramount importance to capture the progress of the flame itself, it is also necessary to consider in detail the nuclear reactions that go on in the ash after the flame has passed. These are important not only to the nucleosynthesis, but to the dynamics. While the net burning from fuel to ash is always exoergic, there are several phases to consider. First, carbon and oxygen burn isobarically in the flame to a given composition that, at high temperature in nuclear statistical equilibrium (NSE), may contain substantial helium and protons from photodisintegration (the protons come especially from the photodisintegration of ⁵⁶Ni into ⁵⁴Fe + 2p). This NSE composition continues to evolve in response to the changing temperature and density after the flame itself has passed. If the temperature goes down or the density up, reassembly of photodisintegration products, especially helium, can give a large energy yield. Conversely, if the temperature increases or density declines too rapidly, the energy generation can be locally endoergic as iron-group elements are photodisintegrated to light species. Generally, adiabatic expansion gives a large positive energy generation because the decreasing temperature has a larger effect than the declining density. In addition, electron capture changes the makeup of the iron group turning ⁵⁶Ni into ⁵⁴Fe and ⁵⁸Ni and even ⁵⁶Fe. These more neutron-rich nuclei are more tightly bound, so electron capture tends to increase the energy yield, but it also decreases the electron density and pressure causing the matter to be compressed and less buoyant.

Figures 11 and 12 illustrate the evolution of various quantities from $t = 0.65$ s (top row) to $t = 0.8$ s (bottom row) in a typical run (specifically, model AV here). Figure 11 shows BE/A in the range [7.82,8.68] MeV/nucleon in the left column and Y_e in the range [0.47,0.50] in the right column, with the color maps increasing from blue to red/pink. Figure 12 shows $T_9 = T/10^9$ K in the range [2,9] in the left column and $X(^4\text{He})$ in the range [0.0,0.25] in the right column.

Initially burning produces a very high temperature and yields a composition with comparable amounts of helium and iron-group elements. This gives a relatively low prompt energy yield as seen in the plot of BE/A, but creates ashes that can yield more energy upon later expansion. This is apparent in the low value for BE/A in the tail of the rising plumes in Figure 11. Later however, the burning goes to lower temperature and produces less helium and greater BE/A as in the bottom left panel of Figure 11. This is most apparent along the rising head of the ashes where the temperature is lowest and recombination has gone the farthest. This reassembly creates a fountain effect in that matter rising along the axis

of the plume gets an extra boost of energy that causes greater expansion and more rapid floatation. The expansion gives more cooling and therefore still more energy generation. As expected, the greatest amount of electron capture occurs deep in the star where the density is high. The electron mole number, Y_e , reaches a minimum of 0.467 there. Burning at lower density gives Y_e very close to 0.50, its initial value for a mixture of ^{12}C and ^{16}O . However there is still substantial neutron-rich material in the outer part of the star along the axis of the rising plume due to the fountain effect mentioned above. Upon ejection this material will be ^{54}Fe and ^{58}Ni , not ^{56}Ni .

4.2. Series B and C: Artificial Ignition Locations

To observe the effect of buoyant bubbles under slightly different conditions, we artificially moved the ignition spot closer to the center of the star where the flow pattern is different from the nearly radially outward flow field from Model AV. Furthermore, the decrease in buoyancy force as the ignition point is placed closer to the star’s center implies that the bubble should interact with the background turbulence for a longer period of time before the bubble rise speed becomes comparable to the background velocity.

Figure 13 shows slices of the fluid speed for models BV (top row) and B0 (bottom row) at three different times (from left to right): $t = 0.1, 0.2,$ and 0.3 s. The blue color scale logarithmically spans ≤ 10 km s $^{-1}$ in black to 10^4 km s $^{-1}$ in white; the red contour marks the flame surface. For each plot, the center of the star is located at the center of the bottom edge, and each edge spans 280 km. As stated in Section 3, the ignition point was placed 10 km off-center — i.e., from the bottom of these slices. The initial burning is laminar at around 95 km s $^{-1}$, but the bottom of the bubbles only expand about a kilometer radially inward before stalling against buoyancy. These bubbles do not burn back through the center, even in the case where there is no initial velocity field (B0); this is in contrast to the resolved study of buoyant flames in simplified, constant gravity backgrounds of Zingale & Dursi (2007).

The presence of the strong non-radial initial velocity component near the ignition location of Model BV is clearly visible. In these slices, the background velocity has a general flow that is towards the upper left corner of the frame, which is along the direction of the stretch and deformation of Model BV at later times. It should be noted that the same ignition shape was used in the B series runs as in the A series; however, the overall orientation with respect to the local gravity vector is different between the two series. In particular, two of the more dominant spherical perturbations to the initial spherical flame surface are seen in this particular viewing angle as the two nodules on the lateral sides of the flame at $t = 0.1$ s in both models. These tend to burn somewhat laterally away from the bulk of the bubble

before buoyantly rising and becoming distorted by the turbulent wake of the leading edge of the flame.

Figure 14 shows similar slices as in Figure 13 but now for Models CV (top) and C0 (bottom) at $t = 0.1, 0.2,$ and 0.4 s from left to right. The color scale here spans from under 1 km s^{-1} (black) to 10^3 km s^{-1} (white). In these panels, the center of the star is at the center of the image, and each edge of the panel spans 150 km . As in series A and B, the bubble quickly burns through the initial perturbations. In the case of no background flow field, Model C0, the flame remains nearly spherical in its early evolution, until it begins to interact with the velocity field generated from its own expansion. In the presence of the background velocity field, Model CV shows a highly distorted flame surface that takes on a shape consistent with the general directionality of the initial velocity field. The very early evolution of centrally located bubbles — during the time period where the local buoyant rise/expansion speed is less than the turbulent intensity — will likely play a role in determining the degree of asymmetry of the explosion. Given that ignition calculations show a non-isotropic convective flow field (Kuhlen et al. 2006; Zingale et al. 2011; Nonaka et al. 2012), it is likely that even if ignition of a perfect sphere occurred at the exact center of a white dwarf, the subsequent deflagration should be highly asymmetric.

Figure 15 compares the nucleosynthetic yields of iron-group elements (top row) and IME (bottom row) as a function of time for both the B series (left column) and C series (right column) of simulations in a similar fashion as Figure 10 for the A series. Again, the dashed grey line shows the percent difference where positive values indicate when the model without the background flow field has produced more material than the model with an initial velocity field. Note that the total mass produced in these simulations is significantly less than that of the A series because they were not evolved nearly as far. With the exception of iron-group elements in the C series of models, both series show a clear trend towards the models with a convective flow pattern producing increasingly more material than the simulations with a static initial velocity field. Furthermore, the percent differences seem much larger here than in the further off-center simulations of A series seeming to suggest that the turbulence affects the burning more strongly for more centrally located ignition. For Models CV and C0, the iron-group element yield curves have similar percent differences and relative slopes as those found for series A (top of Figure 10) where the subsequent evolution reversed the roles, and the model without the initial convective flow pattern ended up producing more material.

4.3. Comparison To Analytic Thermals

Based upon resolved simulations of small-scale burning thermals, Aspden et al. (2011) developed a one-dimensional model of reacting, buoyant bubble evolution. The model was then extended to a full star environment where background stratification becomes important for governing bubble expansion. Aspden et al. (2011) then used the extended model to compare to three-dimensional calculations similar to simulations presented here, though the simulations in Aspden et al. (2011) were less resolved and started with a larger ignition spot. The reader is referred to the Aspden et al. (2011) paper for details, but here we give a brief review of their one-dimensional model for comparison with our three-dimensional simulations.

The general idea of the Aspden model is that there exists a *spherical* bubble of radius (to use the Aspden et al. 2011 notation) b and *uniform* density ρ whose center of mass is located a distance z from the star’s origin. This bubble is buoyantly rising, with speed u , through a stratified, hydrostatic background of fuel with density ρ_f and gravitational acceleration g . The fuel is also assumed to be governed by a relativistic degenerate polytrope of order $n = 3$ ($\gamma = 4/3$), which, when combined with the equation of hydrostatic equilibrium, yields a Lane-Emden equation that requires numerical integration. The fuel within the flame front is assumed to be burned instantaneously to ash with density ρ_a . One can then write a simple set of coupled evolution equations for z, g, ρ_f, b, ρ , and u that take into account entrainment, stratification, and the effective gravity as fuel is burned to ash. The model has two parameters, which are calibrated in their paper: 1) $\alpha = 0.17$, which is the ratio of the entrainment rate to the bubble rise speed, and 2) $\beta = 0.5$, which is an empirical constant that relates the bubble’s effective buoyancy to acceleration of the center of mass of the bubble.

To apply this model to our three-dimensional simulations, we must first determine the initial conditions. We find the bubble’s properties by finding those zones inside the bubble, defined by $X(\text{C}^{12}) \leq 0.1$. We then integrate the quantities $1, \rho$, and ρr over this region to obtain the bubble’s volume, mass, and center of mass location, respectively. At a time, t_0 , when the bubble is well-formed, we use the bubble’s mass and volume to obtain its initial radius, b_0 , and density ρ_0 , assuming it to be a sphere. The initial location, z_0 is given by the bubble’s center of mass location, and the initial velocity, v_0 , is taken to be the center of mass velocity at $t = t_0$. From the star’s central density and pressure, we can determine the normalization constant for the polytropic equation of state, and then the Lane-Emden equation can be integrated to obtain g_0 and $\rho_{f,0}$ at z_0 , thus completing the initial conditions. Table 2 shows the initial conditions used for the semi-analytic models for both simulations in the A series.

One also needs to specify how the density jumps across the flame — how ρ_a changes as a function of ρ_f . Aspden et al. (2011) fit a power law to the properties of laminar flames from Timmes & Woosley (1992). Here, we use a power law fit to the valid density region of the results from flames of Ma et al. (2013), on which our burning network and thickened flame are based. Our power law takes the form $\rho_a = 0.168\rho_f^{1.075}$.

Figure 16 shows the application of Aspden’s model to our Model A0 (left column) and Model AV (right column) data. The three-dimensional data are given as blue crosses, while the lines mark Aspden’s model with different parameters integrated until $t = 1$ s. The red lines are Aspden’s model using the fit parameters as described above. The one-dimensional model is most sensitive to the choice of the empirical constant, β , which governs the fraction of buoyancy that goes towards moving the bubble’s center of mass. The green and black curves show the effects of changing β from its initial value of 0.5 to 0.75 and 1.2, respectively. Each of the parametrizations follows the general trend of the bubble height as a function of radius (top row), including the turn-over as the bubble reaches lower density where steep density gradients exist. It is immediately clear, however, that the original parametrization from Aspden et al. (2011) simply does not rise quick enough compared to our simulations. This fact is more evident in the plots showing the evolution of the bubble’s height as a function of time (middle row). None of the parametrizations tend to rise nearly as quickly as our three-dimensional simulations. As expected, a larger value of β increases the rise speed, and indeed the $\beta = 1.2$ curve comes closest to the three dimensional data, although its gradient is much steeper towards the end of the integration. In terms of the total mass burned (bottom row), all parametrizations do a decent job tracking the three-dimensional results. None of them, however, reproduce the sudden (more so in Model A0) increase in height after $\sim 10^{-3} M_\odot$ of material has burned and the bubble entered a lower density region where the burning takes on a different behavior.

The semi-analytic model has several simplifying assumptions that make the inherently three-dimensional problem tractable, namely:

1. the bubble is always a sphere of radius b ,
2. the bubble has a uniform density, ρ , at any given time,
3. the bubble entrains fuel at a rate proportional to it’s rise speed with proportionality constant α ,
4. the only burning is that which occurs in the vicinity of the flame’s surface, instantaneously changing fuel to ash,

5. and the bubble rises isentropically such that the pressure equilibrium is maintained with the ambient fuel.

Here we discuss the validity of these assumptions as applied to the interpretation of the differences between the model and simulation data.

The first assumption — sphericity — is certainly only valid at early times as evidenced by Figures 6, 7, and 8. Indeed, given the same volume, a plume-shaped object will experience less fluid drag than a perfect sphere, and should thus rise more quickly as is the case of our simulation data compared to the one-dimensional model. The second assumption — uniform density — is also only valid early on, with the error worsening during the evolution, but at a much slower rate than the error from the first assumption.

The third assumption is reasonable to first order — one expects the amount of fuel crossing the flame front to be proportional to the expansion rate of the front through the fuel. In the presence of turbulence the flame front becomes wrinkled, and in the same way that the increased surface area effectively increases the burning rate, so too will the entrainment be increased. The degree of turbulent entrainment will also increase with the decrease in density as the bubble transitions from the laminar to the flamelet to the distributed burning regimes. Therefore, even though the buoyant bubble will reach a terminal velocity, the turbulent entrainment rate is likely (on average) a monotonically increasing function with time until the density is low enough that reactions cease. This effect may, in some sense, be captured by using a turbulent flame speed instead of the constant assumed in both our three-dimensional simulations and the Aspden models. A possible alternative assumption would be to say that the entrainment rate was proportional to some turbulent velocity in the vicinity of the flame. One then has the difficulty of forming a meaningful average over the flame’s surface of this turbulent velocity to use in the one-dimensional model. We found no such simple model, but save this for further exploration.

The fourth assumption — instantaneous, local burning— is certainly not the situation within our three-dimensional simulations. As outlined in Section 2.2, there is an extensive amount of burning that occurs in the ashes of the flame (see also Figures 6, 7, and 8). These reactions will slightly alter the local density, feeding back into the violation of the second assumption. It is not entirely clear how this affects the bubble’s buoyancy, on average, over the course of its evolution.

The last assumption — isentropic rise — is likely quite accurate until the bubble has expanded enough such that the sound crossing time becomes comparable to the timescale for heat diffusion across the bubble, and a lateral pressure gradient forms. This gradient then causes significant lateral expansion, which is not captured by the model. This disparity

is evident in plots of height versus radius (top row) of Figure 16 where the simulation data has a stronger turnover compared to the models once the spherical bubble is about 100 km in radius.

4.4. Characteristic Evolutionary Phases

During its evolution, the burning bubble goes through several phases that can be characterized by their geometry, especially their solid angles, Ω , as viewed from the center of the star. The solid angle, since it generally increases here, is related to the total amount of material being burned at a function of time. That is, for a given star and flame physics, a larger *initial* solid angle will give more burning. This simplification neglects secondary effects, such as the degree to which the burning rate is decreased due to the lower density if significant expansion occurs, i.e. central ignition. For off-center ignition though, such a parametrization is robust.

The solid angle of a spherical cap is given by $\Omega = 2\pi(1 - \cos\theta)$, where θ is the angular radius of the cap in radians. Central ignition, if it continued to burn isotropically, would have $\Omega = 4\pi$, but the solid angle resulting from off-center ignition is much smaller. Figure 18 shows the evolution of the bubble’s solid angle as a function of time for Model AV (red), Model A0 (blue), and the one-dimensional model based on simulation AV with varying values of the empirical constant β (black). The curves for the one-dimensional model based on simulation A0 look similar. The thin, grey vertical lines separate the five distinctive phases of the bubble’s evolution to be discussed.

During the first phase ($t \lesssim 0.05$ s), the evolution is dominated by laminar burning. Since the density and pressure are very nearly constant, the bubble burns isotropically at a constant laminar speed producing a sphere. Little buoyant rise or distortion occurs (e.g. Figure 3). For Model A, after the initial laminar phase, which burned through the imposed surface perturbations, but just before the flame began to float rapidly ($t \sim 30$ ms), its solid angle was $\Omega/4\pi = 4.4 \times 10^{-3}$. For comparison, the 3B25d100 and 3B25d200 models of Röpke et al. (2007b) had *initial* solid angles at ignition of $\Omega/4\pi = 1.5 \times 10^{-2}$ and 3.86×10^{-3} , respectively, and Model N1 of Seitenzahl et al. (2013) had $\Omega/4\pi = 1.8 \times 10^{-2}$. The series of single-point, off-center models of Jordan et al. (2008) had values that ranged from 6.28×10^{-3} to 1.10×10^{-1} . As we shall see, a smaller solid angle implies that less burning occurs in the deflagration, especially early on.

During the next phase ($0.05 \lesssim t \lesssim 0.1$ s), buoyancy becomes important, and by 0.06 s, the bubble’s surface has become elongated along the radial direction. Its top is rising faster

than the local laminar speed. As it becomes increasingly distorted, the bubble takes on the characteristic mushroom shape of Rayleigh-Taylor instability while the effects of turbulence remain small. Although the flame is still expanding laterally via burning, the increase in solid angle slows during this phase due to the accelerating radial floatation.

The third phase ($0.1 \lesssim t \lesssim 0.18$ s) is characterized by the formation and evolution of a single dominant torus quite visible in a plot of vorticity (see the first panel of Figure 5). Buoyancy still pushes the widest part of the bubble to larger radii, but there is also a brim forming near the bubble’s top as the flame begins to roll into itself. Around $t = 0.14$ s, buoyancy dominates sufficiently that the solid angle reaches a local maximum. At about the same time, the high-vorticity brim of the bubble has become well-formed. Up until this point, the widest part of the flame — the part that sets the solid angle as seen from the center of the star — occurred at a distance somewhere near the middle of the bubble’s radial extent. Between $t = 0.14$ and 0.17 s, however, the brim of the bubble undergoes a single overturn, rolling the flame surface such that the widest part occurs closer to the top of the bubble. This causes an abrupt drop in the apparent solid angle of the flame. Over the next 0.01 s, the brim undergoes a second overturn causing an even sharper drop in solid angle. The torus looks like it is pulsating.

This high-vorticity torus does not remain the only vortex tube for another turnover of the brim, however. Indeed, the next phase ($0.18 \lesssim t \lesssim 0.5$ s) marks the transition to turbulence as the single torus breaks down into several vortex tubes. These tubes initially lie near the brim and upper regions of the flame surface, but later progress into the ash. During this period, the flame expands in a nearly conical, self-similar fashion with a nearly constant solid angle. There are small fluctuations about the constant solid angle as roiling turbulence in the cap occasionally causes large-scale wrinkles to form on the surface, such as those seen in Figures 6, 7, and 8. These turbulent fluctuations are experienced throughout the remainder of the bubble’s evolution as it makes its way to lower density regions, where the final phase occurs.

During the last, fifth phase ($t \gtrsim 0.5$ s), the bubble expands laterally much more rapidly than in its earlier buoyant rise (e.g. top panel of Figure 16). This causes the solid angle to increase dramatically. Of the five phases modeled, most of the burning happens here. Figure 17 shows contours of pressure (left) and density (right) for Model AV at $t = 0.8$ s; each slice is 2400 km on a side, and the red contours are highlighted to aid the eye. Early in the bubble’s evolution — or, equivalently, near the center of the star — the pressure scale height and the sound speed are large. Here the bubble is small and floating slowly so that sound waves have sufficient time to maintain pressure equilibrium across the plume as it ascends. That is, the sound crossing time for the ash is short compared with the time for

the plume to rise a fraction of a pressure scale height. Consequently, near the center of the star, the isobars in Figure 17 are aligned with gravitational equipotential lines, which lie on spheres. Later in the evolution, farther from the center, the situation is reversed. The bubble has become large and is floating at a fraction of the sound speed. The pressure scale height has also become shorter. During the time it takes a sound wave to cross the ash, the elongated plume moves an appreciable distance (compared with the pressure scale height). The isobars at larger radii in Figure 17 thus no longer lie on lines of constant radius across the flame. Sound waves can no longer maintain pressure balance along equipotentials, and pressure gradients form across the flame.

The lateral acceleration from the pressure gradients can be estimated by considering an idealized plume of ash with a maximum cylindrical extent, ΔL , rising through a region with a background pressure gradient $dP/dr|_{\text{fuel}}$. Because the unburned part of the star is not yet expanding rapidly, local hydrostatic equilibrium is still a good approximation, so $dP/dr|_{\text{fuel}} \approx -\rho g$, where g is the local acceleration due to gravity. From the isobars at large radii in Figure 17, one sees that the pressure gradients within the ash are shallower than in the fuel, but still very roughly in hydrostatic equilibrium. It is the difference in these pressure gradients, $dP/dr|_{\text{ash}} - dP/dr|_{\text{fuel}} \approx f\rho g$ that drives the lateral acceleration. The factor $f \ll 1$ is included to account for the difference in radial pressure gradients across the growing flame. Initially f is zero, but it increases as the flame grows. If the local floatation speed is v_{float} , the plume rises a radial distance $\Delta r = v_{\text{float}}\Delta L/c_s$ during a sound crossing time and sees an effective pressure change $\Delta P \approx f\rho g v_{\text{float}}\Delta L/c_s$. The pressure gradient $\Delta P/\Delta L$ thus causes a lateral expansion driven by an acceleration

$$\gamma \approx f \left(\frac{v_{\text{float}}}{c_s} \right) g. \quad (5)$$

The baroclinicity discussed in Section 4.1 (and evident in the misalignment of lines of constant pressure and density in Figure 17) drives turbulence that allows the expansion to digest the entrained matter, but the baroclinicity and the vorticity it drives are both very small in the fuel. The burning expands sideways because it is pushed; the turbulent entrainment digests the fuel that is swept up. The sideways pressure gradient force is no different, in principle, from the floatation caused by buoyancy.

4.4.1. Time Scales and Scaling Relations for Early Burning

The above physical description allows some simple analytic approximations and yields some interesting scaling relations. At sufficiently early times, burning in a bubble close to the star’s center occurs in a region of nearly constant density and pressure. The bubble

experiences a buoyancy force given by the local effective gravity

$$g_{\text{eff}}(r) = \frac{4}{3}\pi G\rho r A_t, \quad (6)$$

where r is the radial distance, ρ the fuel density, and A_t the Atwood number of the flame. Figure 19 shows g_{eff} for our white dwarf using the Atwood number as a function of density given by Timmes & Woosley (1992) (note that the quantity $\Delta\rho/\rho$ in that paper is the difference between density in the fuel and the ash density divided by the fuel density, $\Delta\rho/\rho = 2A_t/(1 + A_t)$; Timmes, private communication). The grey vertical line marks the radius at which our Model A simulations were ignited. For our density profile, the Atwood number is close to 0.1 for radii less than ~ 300 km (about a pressure scale-height), so one may write

$$g_{\text{eff}}(r_7) \approx 7.0 \times 10^8 r_7 \text{ cm s}^{-2}, \quad (7)$$

where $r_7 = r/10^7$ cm. The curve in Figure 19 maintains a linear relationship ($g_{\text{eff}} \propto r_7^{0.92}$) with radius until the density noticeably drops. At the ignition location for Model A, $r_7 = 0.413$, Equation 7 gives $g_{\text{eff}} \sim 3 \times 10^8 \text{ cm s}^{-1}$, consistent with Figure 19.

The bubble initially expands isotropically due to laminar burning. The time scale for floatation to stretch the bubble in the radial direction is roughly equal to the time it takes the bubble to float the same distance it burns, $t_{\text{fl}} = 2v_l/g_{\text{eff}}$. After t_{fl} , the bubble responds to forces that, until lateral pressure gradients develop in stage five (Section 4.4), are strictly radial. Within the first pressure scale height, the near constant density profile yields a constant v_l profile, such that t_{fl} takes on a simple relationship with ignition radius

$$t_{\text{fl}} \approx 27 (r_7)^{-1} \text{ ms}. \quad (8)$$

During t_{fl} , the flame grows in radius by $l_{\text{fl}} = v_l t_{\text{fl}}$ or

$$l_{\text{fl}} \approx 2.58 (r_7)^{-1} \text{ km}. \quad (9)$$

For our ignition radius, Equation 8 gives 65 ms, which is just after the onset ($t \sim 50$ ms) of our qualitative phase two shown in Figure 18. Equation 9 gives an increase in bubble radius during this time of 6.25 km for our ignition radius; the three-dimensional simulations gave an average increase in radius of about 7.75 km at t_{fl} , which agrees with Equation 9 to an accuracy of about 25%. By t_{fl} in the simulation, the bubble has begun to interact with the velocity field generated from its own rise, something that is neglected in the simple scaling analysis analysis.

The quantity l_{fl} sets the grid resolution required to treat the early burning correctly. Whether the burning ignites at a geometrical point or in a spherical region with radius 1 km

does not matter. Laminar burning will quickly turn a point into a sphere of at least this size, but the scale where the bubble starts to float and deform must be resolved. It is promising to note that similar scaling relations for the time scale for float speed to equal flame speed, $t_{\text{fl}}/2$, show that a bubble ignited less than ~ 10 km off-center will burn through the center before it floats away, consistent with more detailed estimates (e.g. Zingale & Dursi 2007).

It is also curious that the solid angle at t_{fl} , $\Omega/4\pi \approx 0.013$ from the simulation, is approximately equal to the near constant solid angle attained later during the turbulent phase four in Figure 18. The local maximum in solid angle is a transient event related to the formation and breakdown of the high-vorticity torus. More simulations are required to determine if this is a general property of burning bubbles in their early evolution or just a coincidence. If this is a property of buoyant flames, then our scaling relations can be used to approximate the solid angle of the bubble before it begins lateral expansion in phase five. Indeed, Equation 9 gives a solid angle at t_{fl} of

$$\frac{\Omega}{4\pi} \approx \frac{1}{4} \left(\frac{l_{\text{fl}}}{r_7} \right)^2 \approx 5.7 \times 10^{-3} \left(\frac{0.413}{r_7} \right)^4, \quad (10)$$

where, as in Equations 8 and 9, r_7 is the *ignition* radius; this is reasonably consistent with the numerical simulation. Equation 10 is also an estimate of the fraction of the star that burns during phase four. The amount of burning during this phase is thus very sensitive to the radius where the initial burning is ignited. In the next subsection, however, we shall see that this sensitivity is diminished by the rapid lateral expansion that happens in stage five.

Different white dwarf models will give similar scaling relations as Equations 7, 8, and 9, just with different normalization constants. The Atwood number and laminar flame speed both have known scalings with density and carbon abundance from Timmes & Woosley (1992). The general trend is that a bubble in a more dense (or carbon-rich) white dwarf will grow larger in size before buoyancy dominates and the bubble moves radially than it will in a less dense (or carbon-poor) white dwarf.

4.4.2. Expansion During Late Burning

The bulk of the energy release and nucleosynthesis occurs during the fifth stage outlined above; indeed, nearly 80% of the burning occurs during this phase (see, Figure 10). As previously discussed, this stage is marked by significant lateral expansion, which allows for the processing of a large volume of fuel, as is clearly seen around $t = 0.5$ s where the solid angle behavior changes abruptly from nearly constant to a profile proportional to t^{3-4} .

The solid angle scales roughly as $\Omega \propto (L/r)^2$, where L is the lateral size of the plume

and r its radial distance from the center of the star. In Section 4.4 it was shown that lateral pressure gradients form within the bubble causing an acceleration γ given by Equation 5. As the bubble grows ever larger, the time for sound waves to communicate the change in pressure to the edge of the bubble grows. The lateral acceleration, γ , itself is *increasing* on a sound-crossing time scale — i.e. f and v_{float} in Equation 5 increase with time. The ratio $c_s/g \approx 0.04$ s is roughly constant throughout the bubble’s evolution. This gives a growth in plume size somewhat faster than that of constant acceleration motion:

$$L \sim \frac{1}{2}\gamma_0 t^{2+n}, \quad (11)$$

where γ_0 is the lateral acceleration of Equation 5 at the start of phase five, and $n \sim 0.7$ from inspection of average values of $f v_{\text{float}}$. The radial distance of the bubble is also increasing with time due to the effective gravitational acceleration, g_{eff} . At the start of stage five, the bubble’s radial distance is $r \sim 475$ km; Figure 19 shows that g_{eff} itself is *decreasing* steeply for larger radii. In a similar manner as in Equation 11, the radial distance of the bubble grows as

$$r \sim \frac{1}{2}g_{\text{eff},0}t^{2-m}, \quad (12)$$

where $g_{\text{eff},0}$ is the effective gravity at the start of phase five, and fits to the data in Figure 16 give $m \sim 0.95$. This yields a solid angle profile of

$$\Omega \propto t^{2(n+m)} \sim t^{3.3}. \quad (13)$$

During phase four, the solid angle is roughly constant with time, $\Omega/4\pi \approx 0.013 \approx 0.25 (L/r)^2$. This implies $v_{\text{lateral}} \approx v_{\text{float}} (L/r)$, where v_{lateral} is the lateral spread speed. At the point when phase four transitions to phase five, v_{lateral} is determined approximately from the derivative of Equation 11. This yields

$$t \approx 0.053 \left(\frac{1}{f_0} \right)^{0.59} \text{ s}, \quad (14)$$

where the float speed cancels out from Equation 5, and we have used the above values for the solid angle and c_s/g . Here, f_0 is the value of f in Equation 5 at the transition from phase four to phase five. At the bubble’s radial distance at the phase four to phase five transition (equivalently, about a third of the way up the flame in Figure 17), isobars slightly deviate from equipotential lines and $f_0 \lesssim 2\%$, small but non-zero. Plugging this into Equation 14 yields $t \gtrsim 0.53$ s, which is close to the transition time of about 0.5 s from Figure 18. This very simple analysis, which ignores some of the finer details of viscosity and shear discussed in Zingale & Dursi (2007), agrees well with our simulation data for our two Model A runs.

While the rapid lateral expansion at the end reduces the strong sensitivity of the mass burned to ignition radius seen in phase four (r_{ign}^{-4}), it probably does not remove it entirely. A plume with a larger solid angle to begin with will begin the rapid expansion associated with phase five earlier since the sound waves will find it more difficult to maintain lateral pressure balance deeper in the star. Additional study is needed to determine the actual scaling (see Dong et al. 2013).

5. Conclusions

We have extended our low Mach number studies of white dwarf ignition with Maestro (Nonaka et al. 2012) into the regime of flame propagation using the fully compressible code, Castro. The new simulations directly map the turbulent convective flow field from the earlier study onto the initial grid to determine its effect on buoyant flame propagation. This allows, for the first time, a study of the deflagration phase of the traditional single degenerate, M_{Ch} -mass model of SNe Ia using a realistic background convective flow field in three dimensions. One goal of this study was to assess the degree to which this realistic flow field would affect the evolution of the buoyant flame as it made its way to the stellar surface. To this end, we used a simple thickened flame model coupled with nuclear reaction tables generated from detailed calculations of isobaric carbon burning plus post-flame burning in the NSE regime, similar to that used in Ma et al. (2013).

We find that the background turbulence from the convective flow field is generally a minor modification to the hydrodynamics, once the burning enters a strongly buoyant phase. Characteristic turbulent speeds from prior convection are comparable to the laminar speed early on, but not to floatation speeds. Thus, except for determining the site where the explosion originates, the turbulence from prior convection does not play an important role in our standard run ignited 41 km off center. However, closer to the center, the buoyancy force is smaller and the bubble interacts with the turbulence for a longer period of time. This leads to more distortion and wrinkling that is compounded by Rayleigh-Taylor instabilities, which grow with time. In the extreme case of central ignition, the background turbulence has a profound effect on the outcome. Since the typical convective speeds and laminar speeds are nearly the same, an outbound eddy can carry an ignited region off-center before its floatation speed becomes dominant. Since hot ignition sites almost universally exist in outflows, not inflows, even “central” ignition becomes non-central and produces an asymmetrical explosion. This makes it even more difficult to burn a large solid angle of the star and cause significant expansion prior to detonation. Less white dwarf expansion implies the detonation burns at higher density, producing more ^{56}Ni and a brighter SN Ia.

At all times, even in the presence of the background flow field, our calculations show that the high vorticity flow indicative of strong turbulence exists only within the ashes of the flame. *There is very little turbulence outside or ahead of the flame.* This could have consequences for more sophisticated turbulent flame models that average the local turbulent fluctuations over some region in the vicinity of the flame to obtain a turbulent flame speed. If the region over which the average is formed includes a large fraction of material outside of the flame, this will result in a turbulent flame speed that is too low, which might alter the total mass burned and the nucleosynthesis.

Using a simplified flame model allows us to compare the evolution of our buoyant flames to one-dimensional semi-analytic work of buoyant thermals presented in Aspden et al. (2011). We find these semi-analytic models approximate the overall behavior of our three-dimensional simulations quite well, although the analytic approximations produce bubbles with somewhat slower rise speeds and not quite enough lateral expansion at later times. A possible remedy to the analytic model’s slower rise speed compared to our simulations, although complicating the simple model, would be to use a non-constant entrainment coefficient (α) or non-constant flame speed, or both. The lack of late time expansion is likely due to the neglect of pressure gradients in the analytic approximation.

Lastly, we find that the buoyant flame bubble undergoes at least five different phases of evolution as it progresses towards the surface. We have distinguished these phases based upon the behaviour of the bubble’s geometric solid angle as seen from the center of the star. In the first phase, the bubble simply burns isotropically at the laminar speed as there is little to no turbulence. After a short time, the bubble has expanded enough that buoyancy starts to dominate the upper cap, causing the bubble to extend radially. This buoyancy-driven phase is ended with the development of significant vorticity in the cap of the bubble. The high-vorticity torus that forms in the bubble creates a brim where the flame rolls over into itself. This tight torus lasts for about two turnover times before splitting up into several smaller vortex tubes, marking the transition to a turbulence-dominated phase. Turbulence is important to the flame’s propagation during the remainder of its evolution. Eventually, the flame reaches a low enough density region where lateral pressure gradients form, leading to the final phase of significant lateral expansion lasting through breakout. These five phases appear to be rather robust as they are experienced by both of our A series simulations. That is, the background turbulence has almost no effect on the presence or duration of these different buoyant flame phases.

The very early laminar burning phase is important as it sets the scale for resolution of the initial floatation and deformation of the flame. Simple arguments relating the floatation speed to the burning speed, show that the early growth of a bubble is inversely proportional

to its off-center ignition radius, out to about 300 km. A point source ignited at a typical off-center ignition location will grow in size to a sphere of radius of a few kilometers before beginning to float. This should be resolved. The solid angle of the ignition point as it starts to float should correlate to the total amount of burning during the deflagration; our simple scaling relations are therefore promising for model parameterization. This behavior appears robust, even in the presence of background turbulence for ignition sufficiently off-center. Closer to the center, turbulence will affect the smooth laminar burning that is assumed in our simple description. Further studies are required to confirm and calibrate the simple arguments made in the text, but it is promising that one may be able to approximately relate the total burning and expansion during the deflagration simply to the ignition radius. We leave this for a future paper.

There is also a very important sixth phase of burning that occurs after the ash erupts from the white dwarf and spreads, at sound speed, over its surface. Hot, light ash is now on top of cold fuel and any Rayleigh-Taylor-based description of the flame is invalid. There is, however, still a great deal of shear between the spreading ash and the fuel beneath. This will drive turbulent mixing that, in the extreme case, might cause detonation, but at a minimum causes continued turbulent burning. Our modeling of this important phase is deferred to subsequent papers. It has been treated previously by Röpke et al. (2007b) and Jordan et al. (2008) among others, but with different results.

If this additional burning is ignored, then our results are consistent with the amount of pre-break out burning seen in a recent similar study of single point ignition by Seitzzahl et al. (2013) (their Model N1). They are also consistent with the relatively small amount of burning seen in this phase by the Chicago FLASH team (Jordan et al. 2008, e.g.) and thus tend to support their conclusion that gravitationally confined detonation will occur in this model. The main underlying cause of the small amount of burning is our previous result (Nonaka et al. 2012) that ignition only occurs once at a single point, well off center.

However, it is possible that the complete neglect of post-break out burning is unrealistic. Different groups treat the uncertain flame physics after breakout in different ways. Some simulations show very little burning at low density ($\lesssim 1\%$) (Dong et al. 2013) while others show substantially more (N1 model of Seitzzahl et al. (2013); private communication). Furthermore, the burning in the surface shear layer mentioned above poses an opportunity for a DDT from shear-heated fuel. Further calculations of the surface burning in a shear layer are needed to settle this important question.

We thank the referee for their thorough reading of our manuscript and their constructive comments. We would also like to thank Andy Aspden for insights into the nature of burning

thermals and his one-dimensional models. We also thank Kalyana Chadalavada for help in getting us (and keeping us) running on the Blue Waters Early Science System. CMM would also like to thank Rob Sisneros and Dave Semararo for discussions of large-scale visualization and the inherent problems therein. Our discussions with Rainer Moll regarding fluid-flame interactions have been extremely insightful, and we thank him. Correspondence with Ivo Seitzzahl was helpful in understanding unpublished details of the MPA models. This research is part of the Blue Waters sustained-petascale computing project, which is supported by the National Science Foundation (award number OCI 07-25070) and the state of Illinois. Blue Waters is a joint effort of the University of Illinois at Urbana-Champaign and its National Center for Supercomputing Applications. This work is also part of the “PRAC Type Ia Supernovae” PRAC allocation support by the National Science Foundation (award number OCI-1036199). Additional computer time for the calculations in this paper was provided through a DOE INCITE award at the Oak Ridge Leadership Computational Facility (OLCF) at Oak Ridge National Laboratory, which is supported by the Office of Science of the U.S. Department of Energy under Contract No. DE-AC05-00OR22725. This research used resources of the National Energy Research Scientific Computing Center, which is supported by the Office of Science of the U.S. Department of Energy under Contract No. DE-AC02-05CH11231. This work was also supported, at UCSC, by the National Science Foundation (AST 0909129), the NASA Theory Program (NNX09AK36G), and especially by the DOE HEP Program through grant DE-FC02-06ER41438. MZ is supported by DOE/Office of Nuclear Physics grant No. DE-FG02-06ER41448 to Stony Brook.

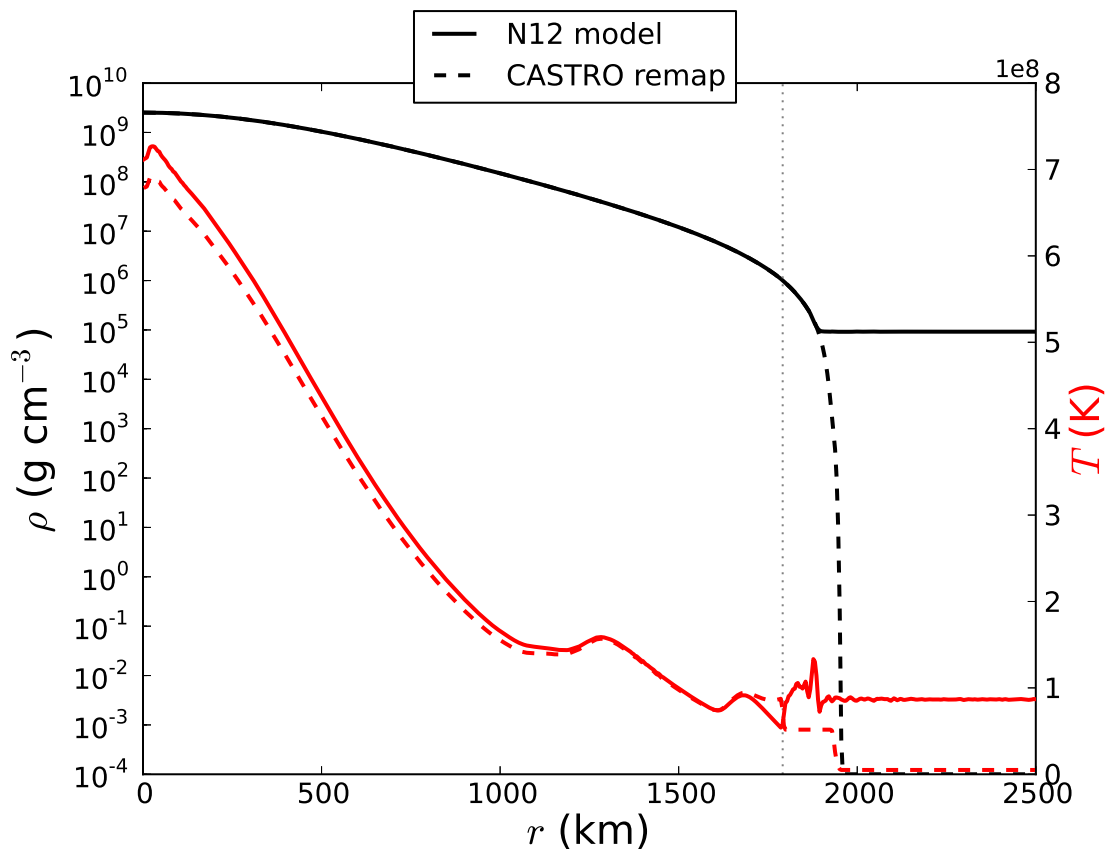


Fig. 1.— Average radial profiles of density and temperature for the N12 model (solid lines) and our mapping of the N12 model into the Castro code (dashed lines). The slight decrease in temperature, especially towards the core, is a result of resetting the composition to a 50/50 mix of carbon and oxygen as described in the text. The vertical dotted line shows the location where we reconstructed a model in HSE.

Table 1: Properties of the various models in this paper.

Model	Initial	$r_{\text{ign}}^{\text{a}}$ (km)	$t_{\text{max}}^{\text{b}}$ (s)	$r_{\text{max}}(t_{\text{max}})^{\text{c}}$ (km)	$M_{\text{IME}}(t_{\text{max}})$ ($10^{-3}M_{\odot}$)	$M_{\text{IGE}}(t_{\text{max}})$ ($10^{-3}M_{\odot}$)	$E_{\text{nuc}}(t_{\text{max}})$ (erg)
	Flow Field?						
A0	N	41.3	0.784	1947	1.46	26.1	3.8×10^{49}
AV	Y	41.3	0.798	1970	1.43	25.8	3.8×10^{49}
B0	N	10.0	0.335	300.8	0.20	2.63	3.5×10^{48}
BV	Y	10.0	0.365	519.3	0.53	6.15	2.3×10^{49}
C0	N	0.00	0.424	53.85	0.02	0.41	3.8×10^{47}
CV	Y	0.00	0.497	101.1	0.05	0.29	7.2×10^{47}

^aOff-center ignition distance

^bMaximum evolution time

^cMaximum radial extent of burning at $t = t_{\text{max}}$

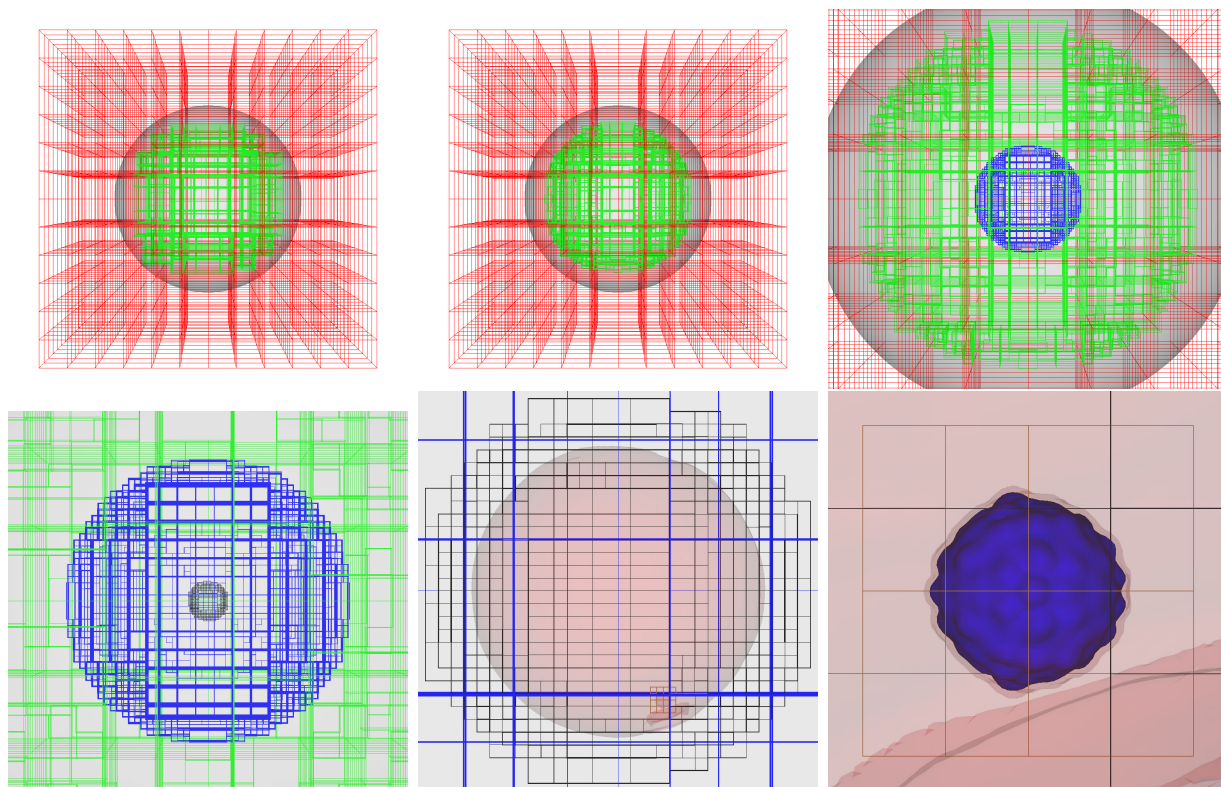


Fig. 2.— Grid layout with each additional level of refinement; each box represents a block of 16^3 to 48^3 zones, depending on the size. The top left figure shows the grid structure for the N12 calculation in Maestro, and the top center figure shows this grid after 20 coarse time steps in Castro. The red and green lines indicate the base ($8.68 \text{ km zone}^{-1}$) and first ($4.34 \text{ km zone}^{-1}$) levels; the grey contour is an isodensity surface at $\rho = 10^4 \text{ g cm}^{-3}$. The next two plots zoom in on the next two levels of refinement, with blue (black) at ~ 1085 (~ 271) m zone^{-1} . The next plot shows the final level of refinement in brown at $\sim 135 \text{ m zone}^{-1}$ and a density contour in red at $\rho = 10^9 \text{ g cm}^{-3}$. The region of ignition is evident in the southeast quadrant. The final figure is a zoom in on the added ignition point where the carbon mass fraction is shown as a blue contour.

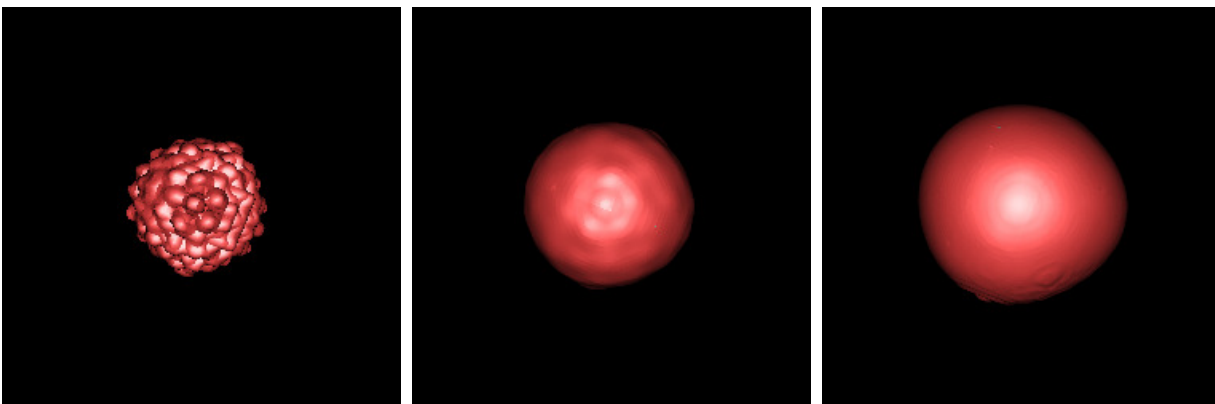


Fig. 3.— Flame surface ($X(^{12}\text{C}) = 0.45$ isocontours) during early evolution of Model AV at $t = 0.00$, $t = 0.0059$, and $t = 0.0119$ s of evolution, from left to right. Each frame has the same spatial scale. The flame quickly burns through the initial perturbations on the top side of the bubble. The direction towards the center of the star is downward in these frames.

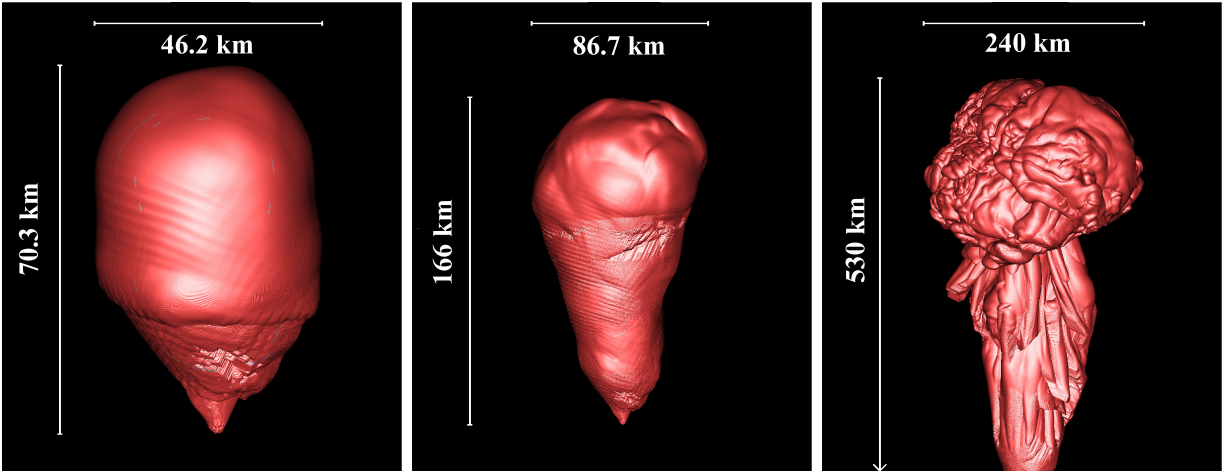


Fig. 4.— Same as Figure 3 — $X(^{12}\text{C}) = 0.45$ isocontours (flame surface) — but at $t = 0.150, 0.265, 0.469$ s from left to right. Each frame has a different zoom level, with the spatial extents of the flame surface indicated. The direction towards the center of the star is downward in these frames.

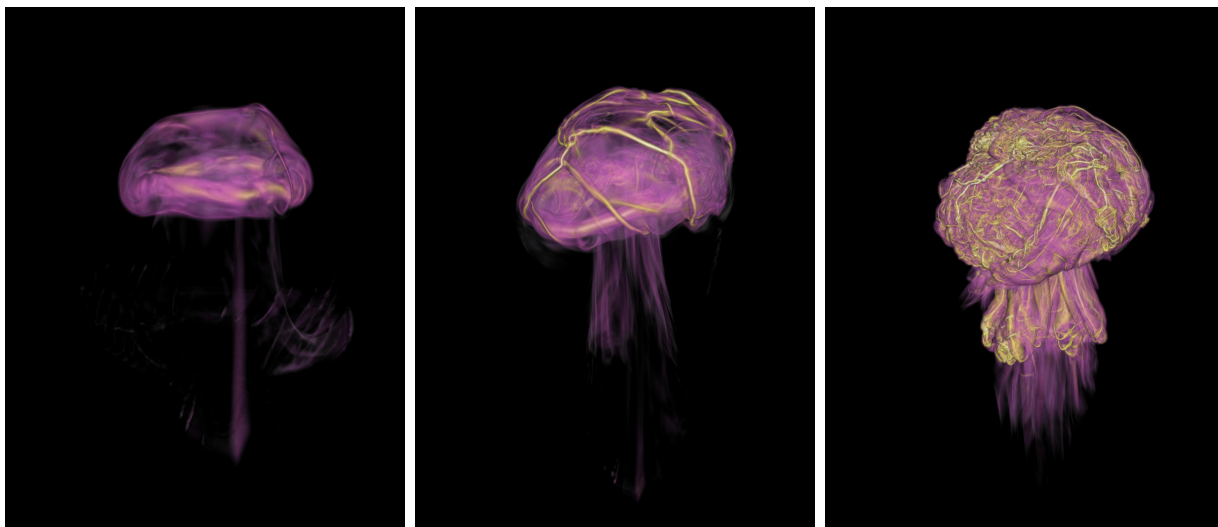


Fig. 5.— Volume renderings of the magnitude of vorticity at the same times ($t = 0.150, 0.265,$ and 0.469 s, from left to right) and spatial scales as in Figure 4. The color scheme goes smoothly from grey, to blue, to purple, to yellow-white as the vorticity increases logarithmically from 100 s^{-1} to several thousand s^{-1} .

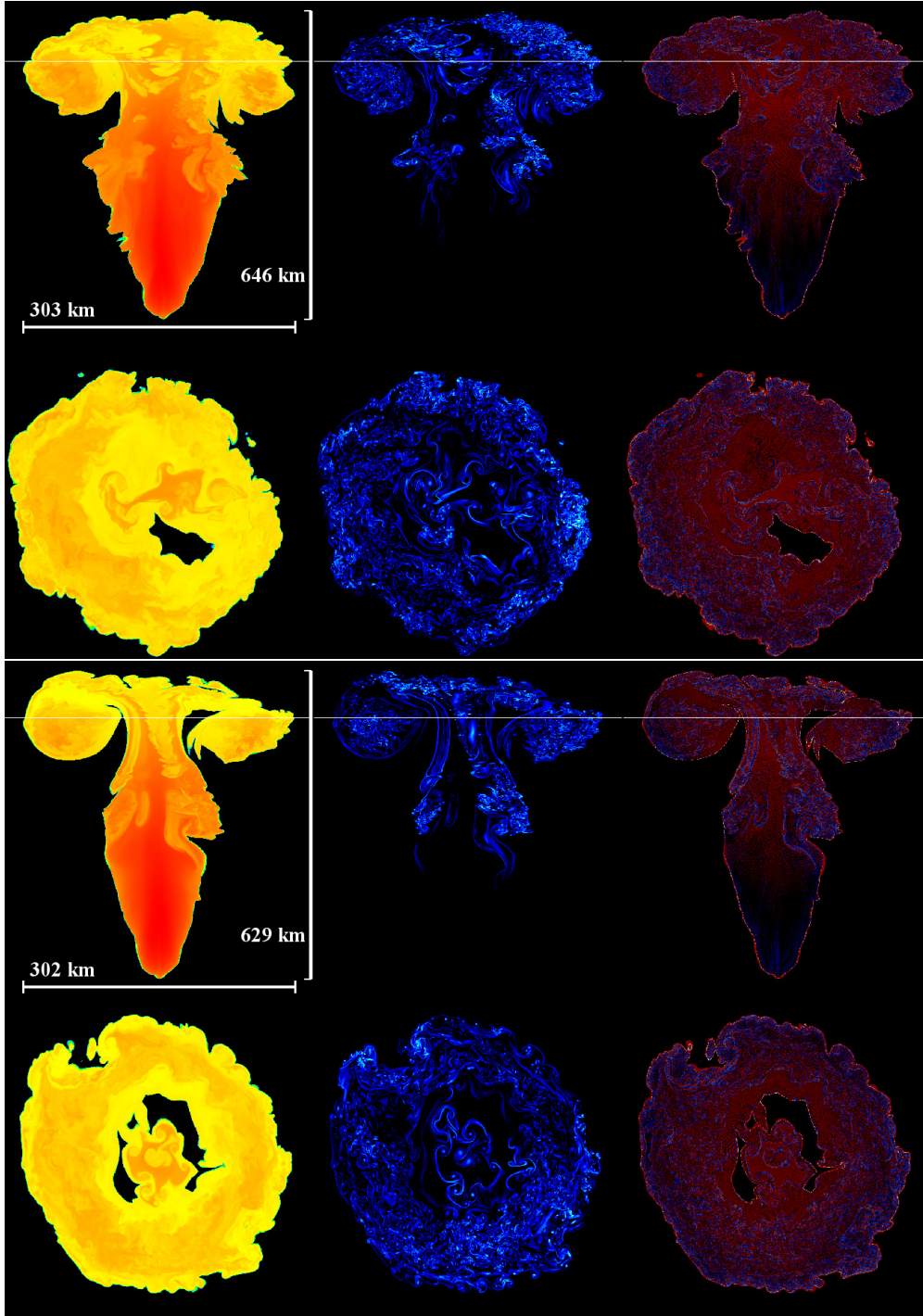


Fig. 6.— Comparison of Model AV (top) with Model A0 (bottom) at $t = 0.5$ s. The columns are, from left to right, temperature (yellow through orange), magnitude of vorticity (blue through white) and energy generation rate (blue for negative values, red for positive). The thin, horizontal white line in the first row of each panel indicates the location of the orthogonal slice shown in the bottom row of each panel. The top row of each panel has an aspect ratio given by the dimensions shown; the bottom rows have an aspect ratio of unity, with the scale given by the width shown.

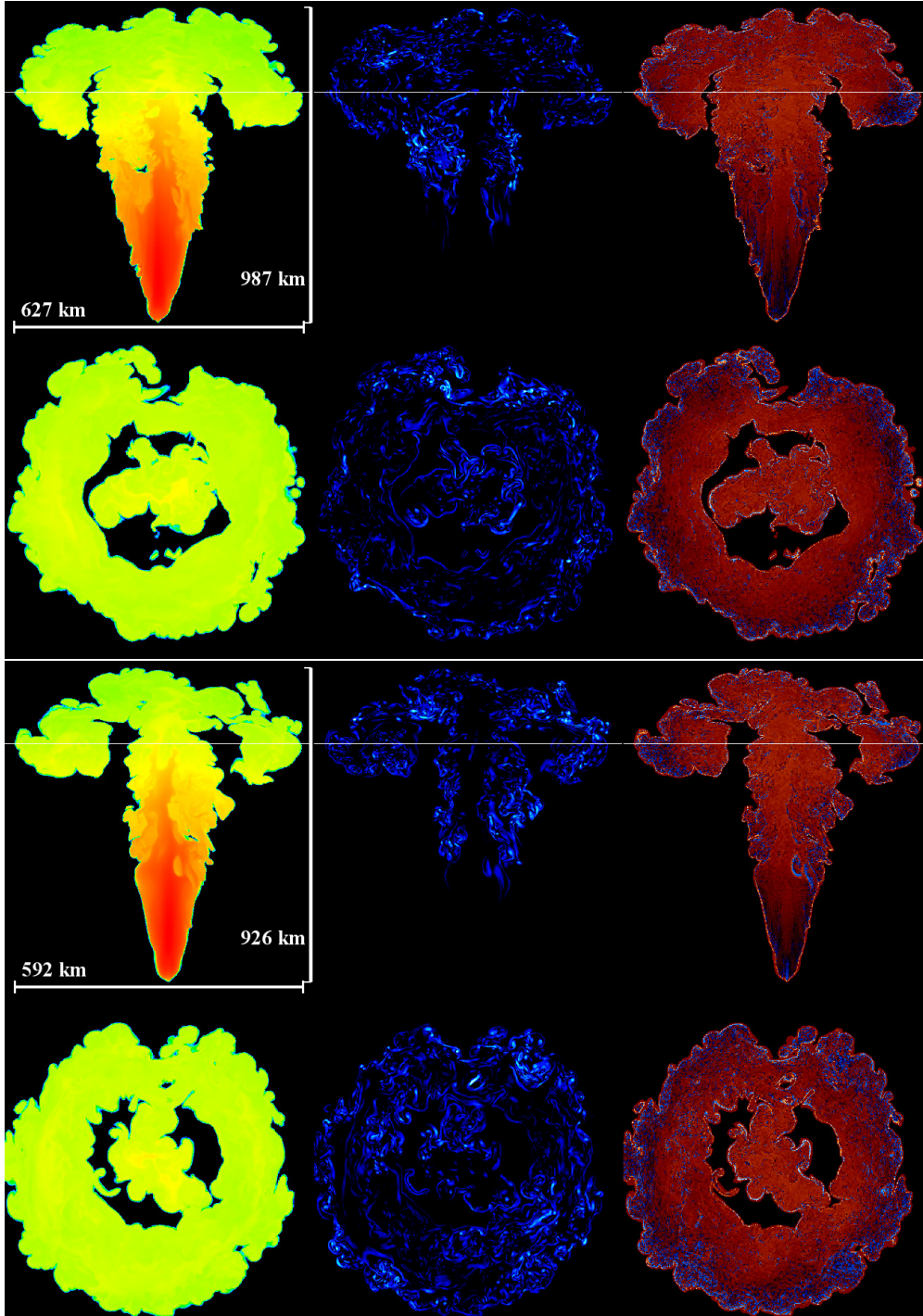


Fig. 7.— Same as Figure 6, comparison of Model AV (top) with Model A0 (bottom), except at $t = 0.6$ s. The columns are, from left to right, temperature (yellow through orange), magnitude of vorticity (blue through white) and energy generation rate (blue for negative values, red for positive). The thin, horizontal white line in the first row of each panel indicates the location of the orthogonal slice shown in the bottom row of each panel. The top row of each panel has an aspect ratio given by the dimensions shown; the bottom rows have an aspect ratio of unity, with the scale given by the width shown.

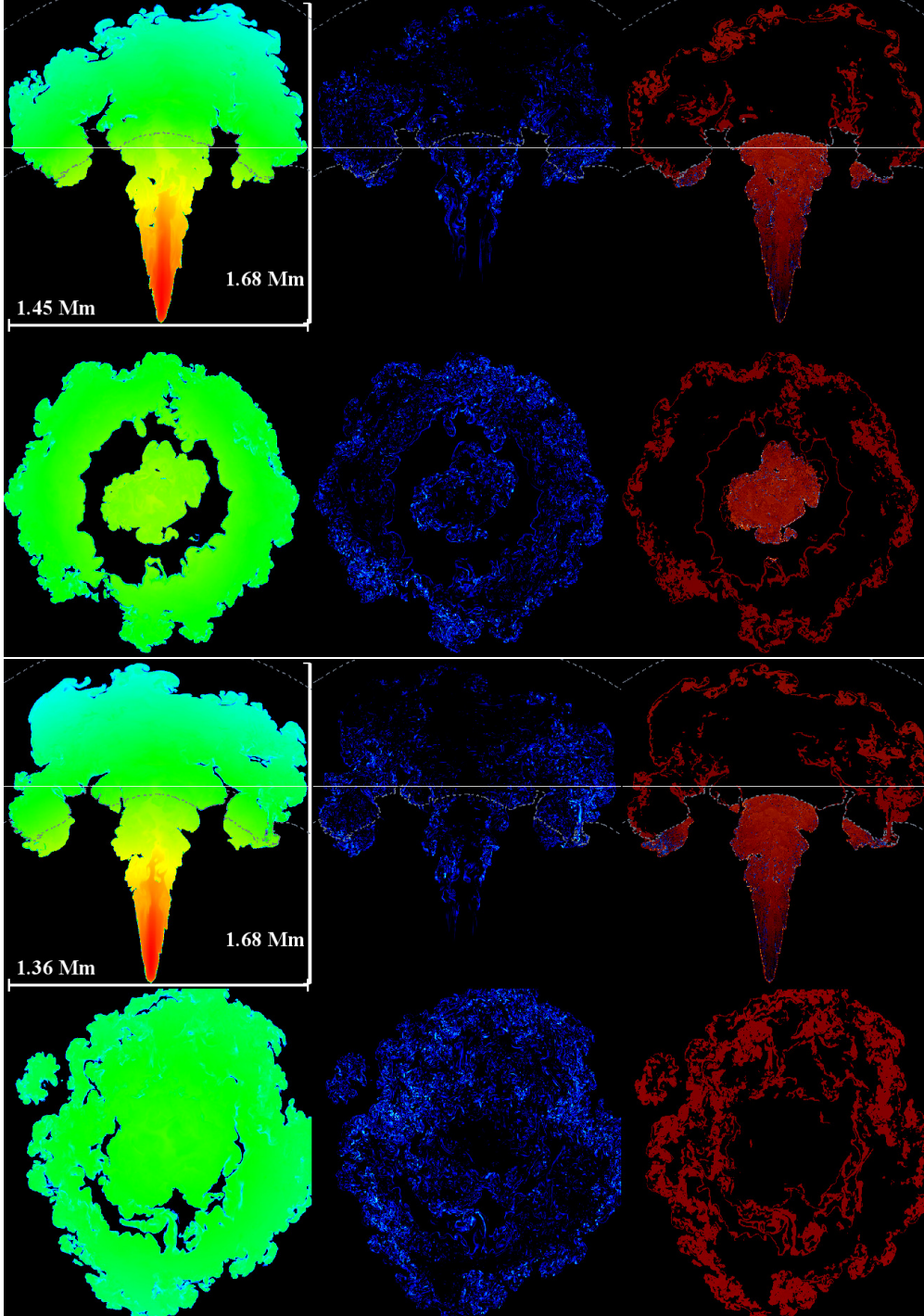


Fig. 8.— Same comparison of Model AV (top) with Model A0 (bottom) as Figure 6 but at $t = 0.75$ s. The columns are, from left to right, temperature (blue through orange), magnitude of vorticity (blue through white) and energy generation rate (blue for negative values, red for positive). The thin, horizontal white line in the first row of each panel indicates the location of the orthogonal slice shown in the bottom row of each panel. The top row of each panel has an aspect ratio given by the dimensions shown; the bottom rows have an aspect ratio of unity, with the scale given by the width shown. The dotted grey lines are contours of density with the inner at $\rho = 10^8 \text{ g cm}^{-3}$ and the outer at $\rho = 10^7 \text{ g cm}^{-3}$.

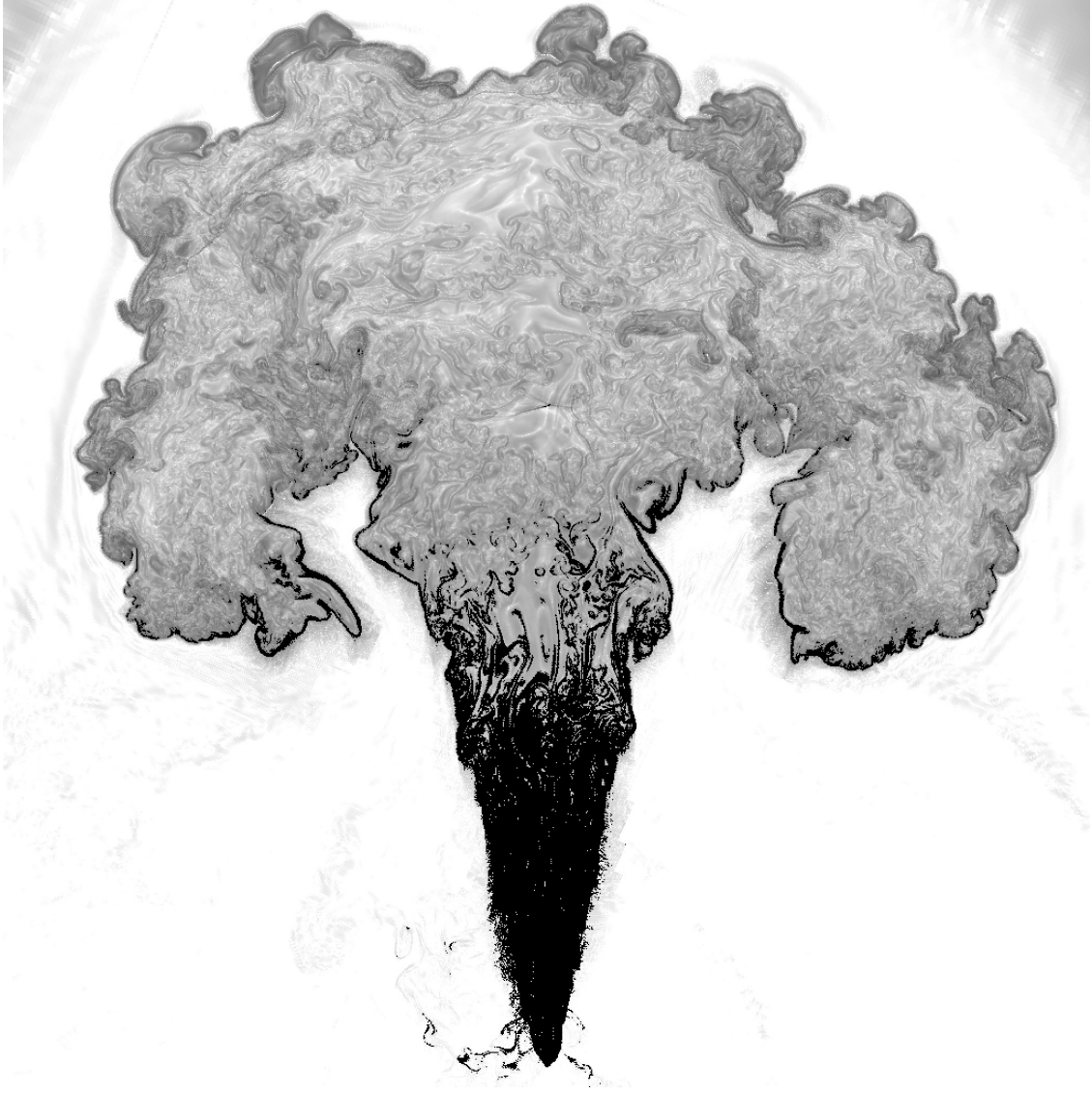


Fig. 9.— Magnitude of baroclinicity, ψ , for Model AV at $t = 0.8$ s. The color map goes from less than 1 (white) to $3.3 \times 10^6 \text{ s}^{-2}$ (black). Baroclinicity is strongest in the tail and underside of the cap, however the relative direction with respect to the flame surface is different in these two regions. In the tail, $\vec{\psi}$ is orthogonal to the flame surface and creates a bulk flow along the direction of the plume in addition to buoyancy. The vicinity of the cap sees $\vec{\psi}$ nearly parallel to the flame surface such that fuel is entrained across the flame front.

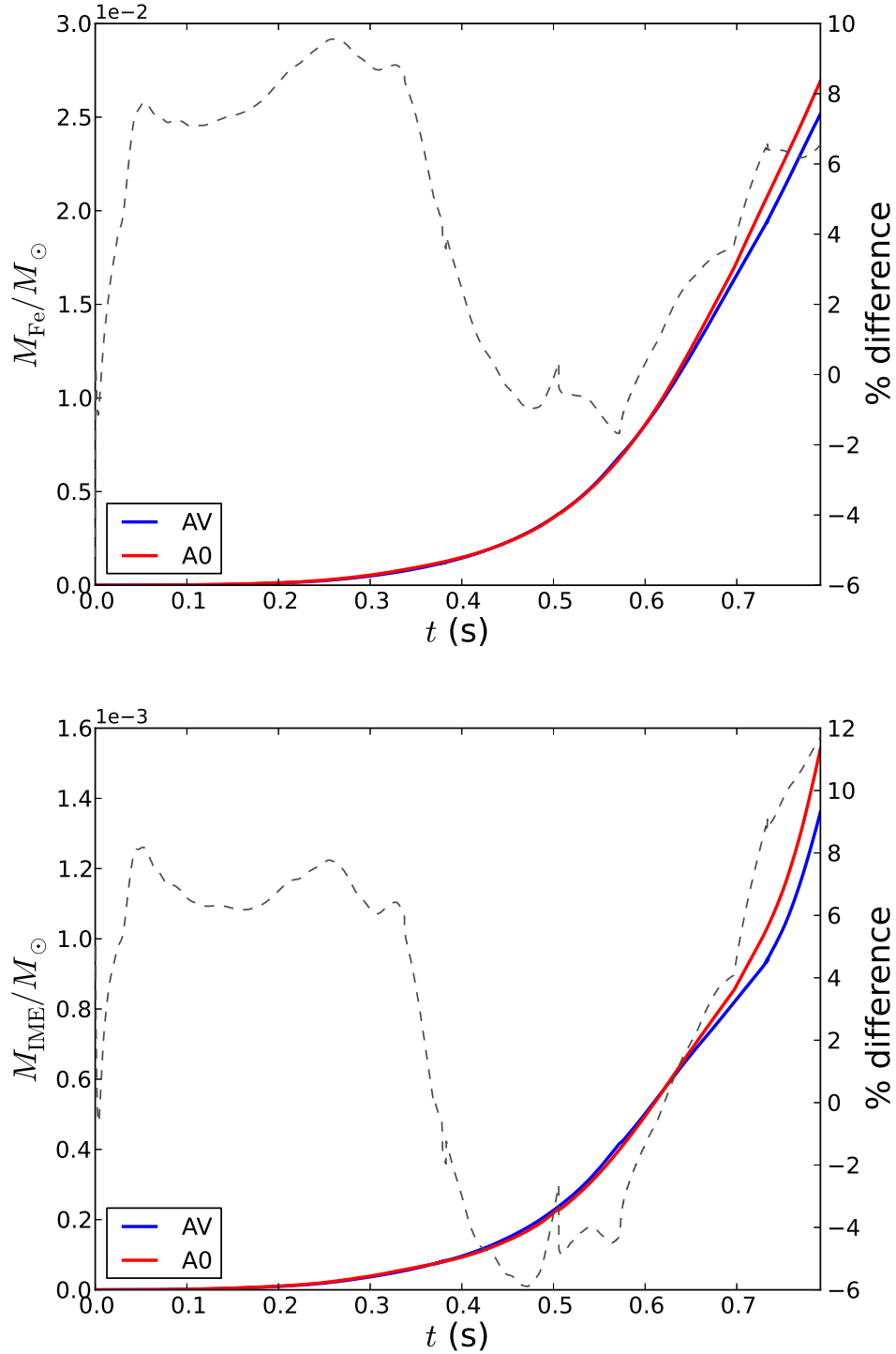


Fig. 10.— Nucleosynthetic yields (left axes) and percent difference (right axes) as a function of time for Models AV (blue) and A0 (red). The top plot shows the production of iron-group material, and the bottom panel shows IME. The percent differences are formulated such that a positive value indicates more production in Model A0 than Model AV. In general, the model without the background flow field (A0) burns more IME and iron-group material.

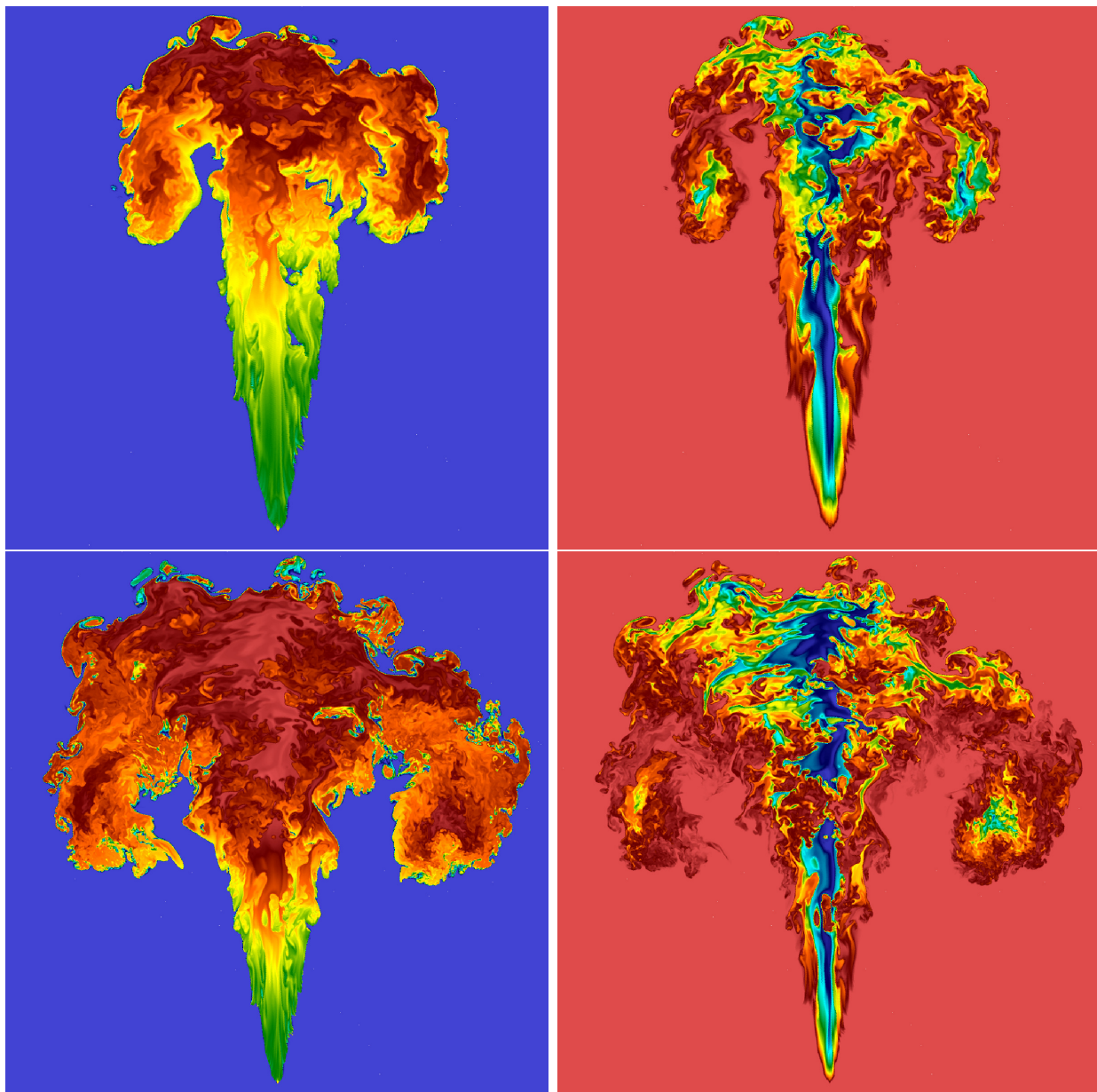


Fig. 11.— BE/A (left column) and Y_e (right column) at $t = 0.65$ s (top row) and $t = 0.8$ s (bottom row) for the standard run AV. The color maps increase from blue to red; for BE/A the range is $[7.82, 8.68]$ and for Y_e the range is $[0.47, 0.50]$. The frames in the top row are 1200 km on a side and those in the bottom row are 2000 km on each side. At early times and in regions closer to the center, the ash temperature is high (Figure 12) and the helium mass fraction is nearly equal to the IGE mass fraction. As the flame progresses to lower densities (bottom row), the temperature in the ash decreases and helium recombination leads to more tightly bound nuclei with larger BE/A . Electron capture prefers higher density, but there is also a significant abundance of neutron-rich material in a narrow plume about the plume’s center, which coincides with the region of tightly bound nuclei. The neutron-rich nuclei now in the outer layers were made deeper in the star and pushed out by a vigorous central flow.

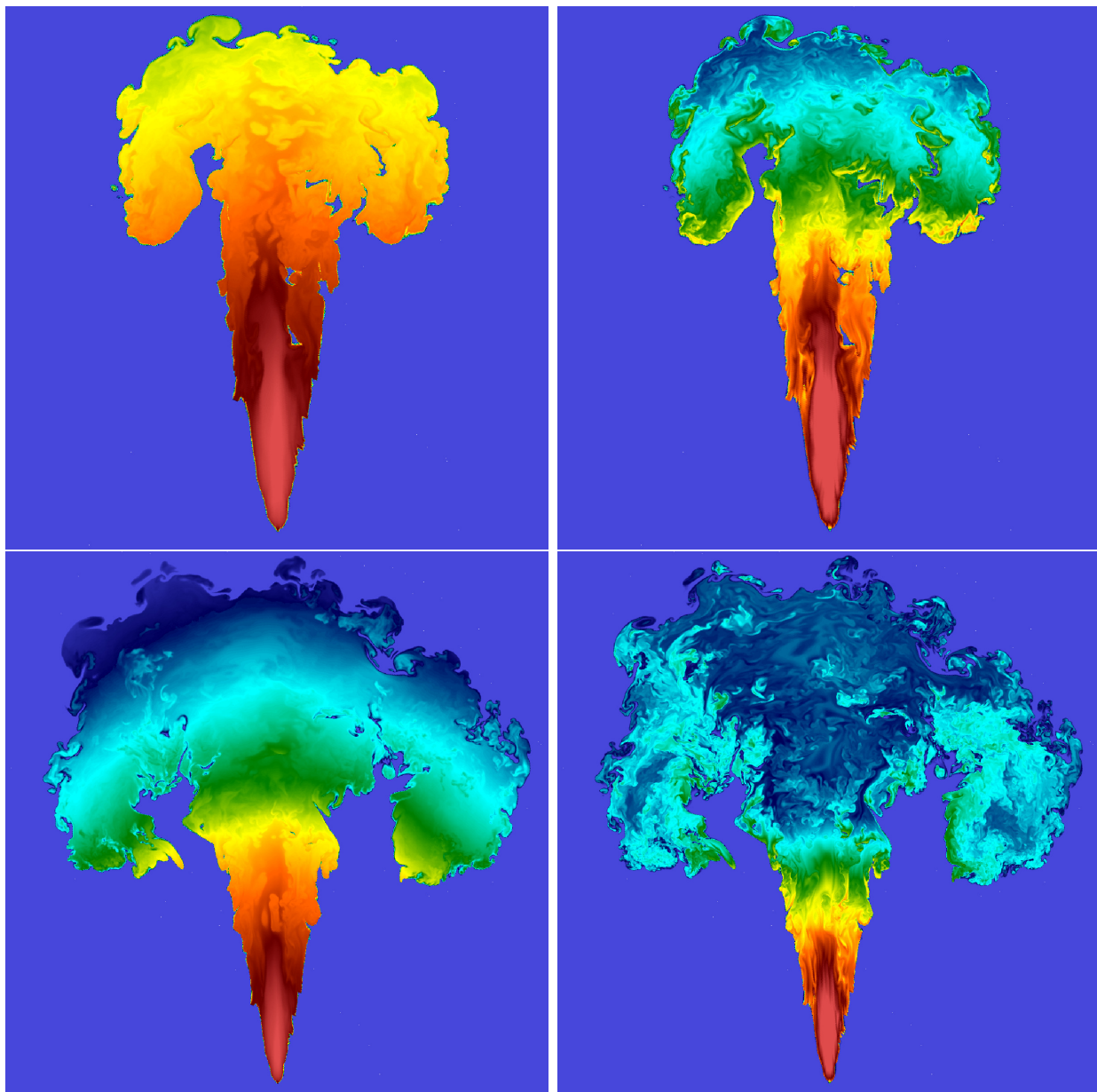


Fig. 12.— $T_9 = T/10^9$ K (left column) and $X(^4\text{He})$ (right column) at $t = 0.65$ s (top row) and $t = 0.8$ s (bottom row) for the standard run AV. The color maps increase from blue to red; for T_9 the range is $[2,9]$ and for $X(^4\text{He})$ the range is $[0,0.25]$. The frames in the top row are 1200 km on a side and those in the bottom row are 2000 km on each side. Note the high degree of correlation between the temperature and helium abundance. In high density regions — either at early times, or in the tail of the flame — large amounts of helium (right column) are produced via photodisintegration reactions because of the high temperature there. At lower density and temperature, recombination occurs leading to a lower helium mass fraction and more tightly bound nuclei (Figure 11). As the flame progresses to lower densities (bottom row), the temperature in the ash decreases and helium recombines giving extra energy to the ash.

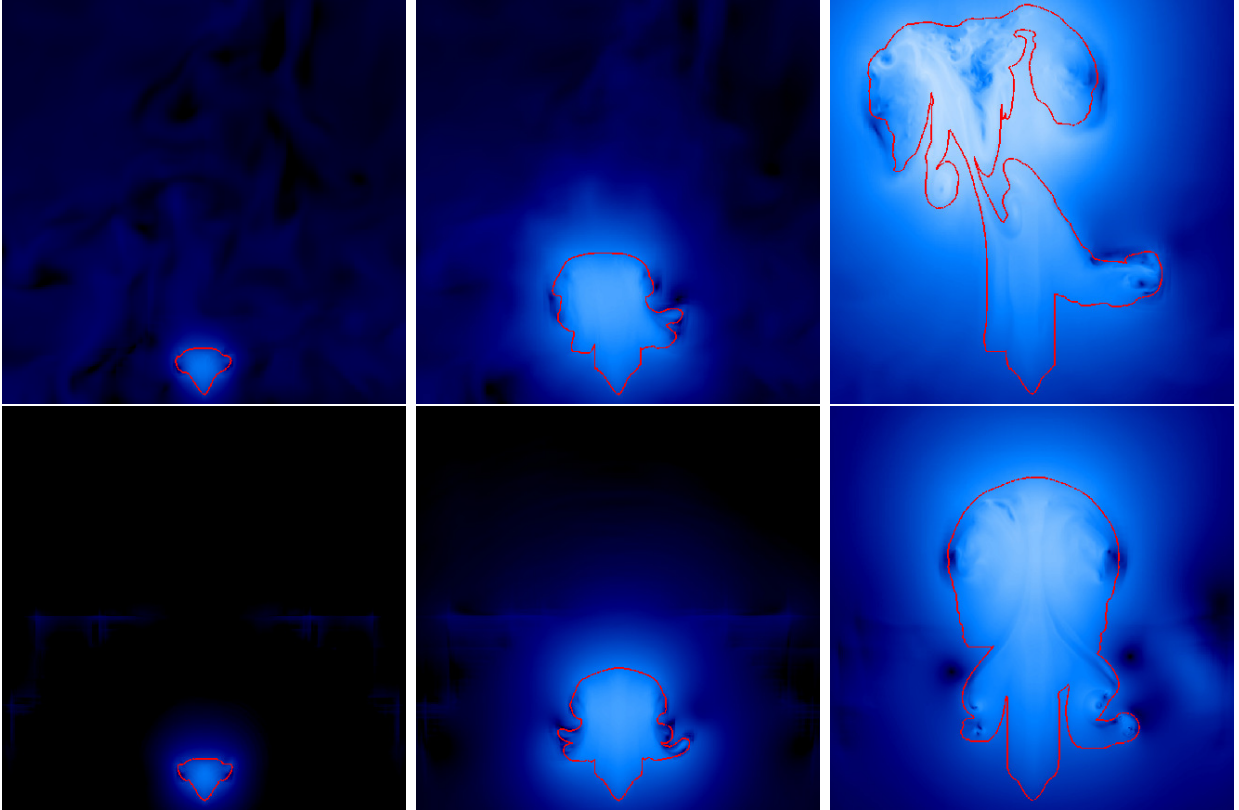


Fig. 13.— Slices in the YZ plane for Models BV (top row) and B0 (bottom row) at $t=0.1$, 0.2 , and 0.3 s, from left to right. The red line is the $X(\text{C}^{12}) = 0.45$ isocontour marking the flame surface. The color plot is the fluid speed, which spans, logarithmically, from less than 10 km s^{-1} (black) to 10^4 km s^{-1} (white). The center of the bottom edge of each panel is at the center of the white dwarf, and all panels have a spatial scale of 280 km on a side. For the BV models (top row), there is a significant non-radial component to the velocity field, as evident by distortion of the flame surface to the upper left of the frames.

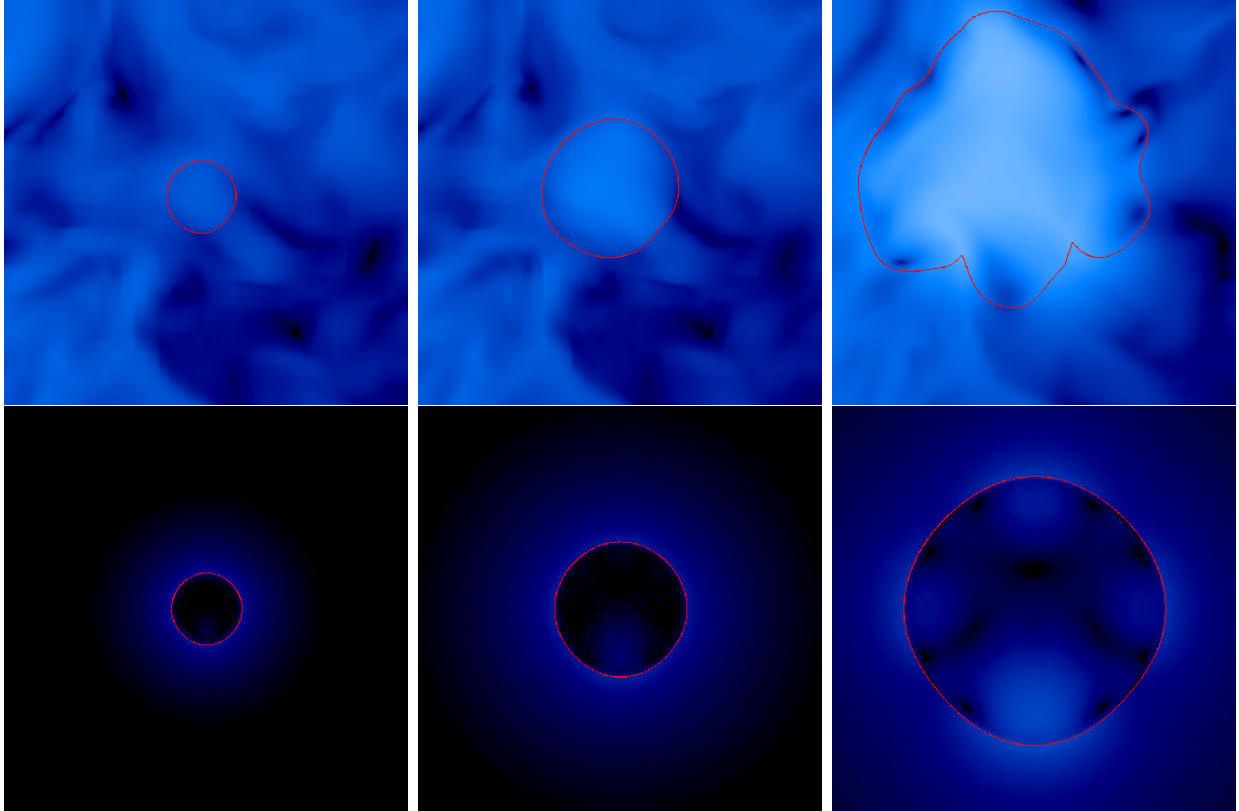


Fig. 14.— Slices in the YZ plane for Models CV (top row) and C0 (bottom row) at $t=0.1$, 0.2 , and 0.4 s, from left to right. The red line is the $X(\text{C}^{12}) = 0.45$ isocontour marking the flame surface. The color plot is the fluid speed, which spans, logarithmically, from less than 1 km s^{-1} (black) to 10^3 km s^{-1} (white). Note the lower maximum speed compared to Figure 13. The center of each panel is at the center of the white dwarf, and all panels have a spatial scale of 150 km on a side.

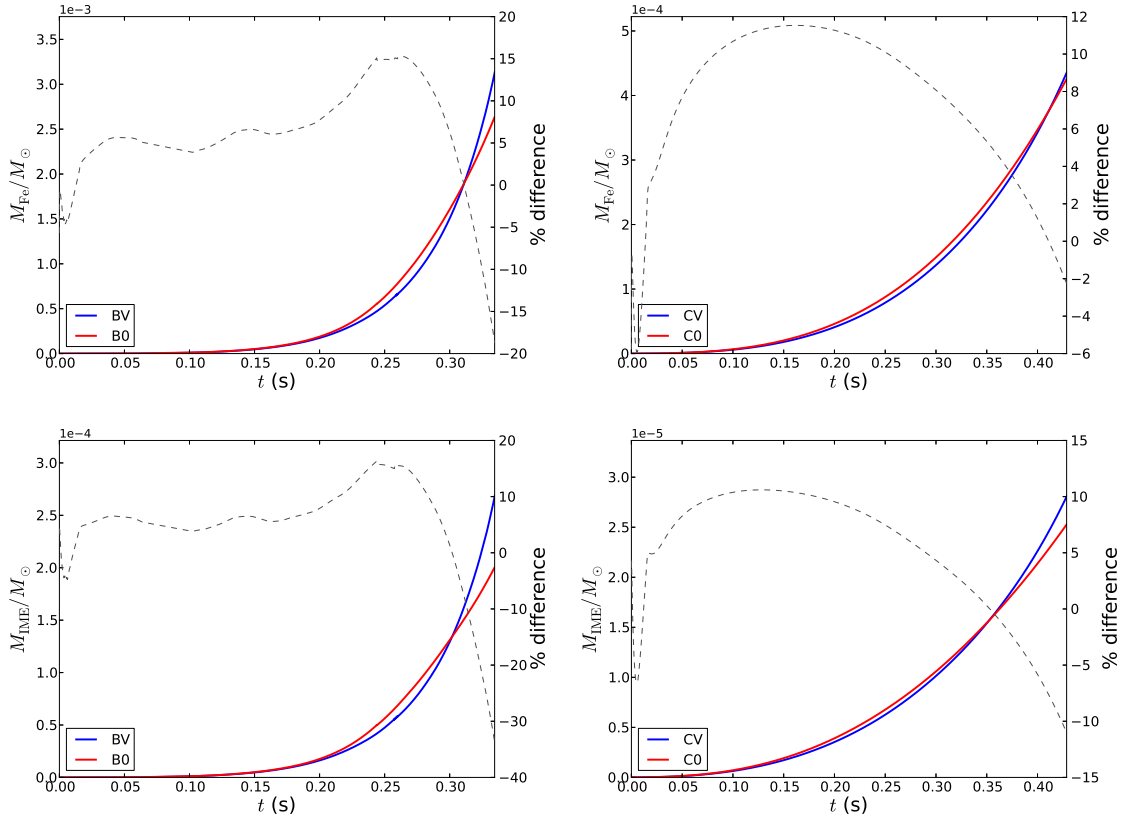


Fig. 15.— Comparisons of nucleosynthetic yields of iron-group elements (top row) and IME (bottom row) for both the B series (left column) and C series (right column). The blue(red) lines correspond to models with(without) a background convective flow field. The dashed grey line shows the percent difference between models with and without the background field; positive values indicate more production in the models without the background field. These plots indicate that the more centrally-ignited models with the background turbulence burn more material than those without, which is in contrast to the further off-center ignition models shown in Figure 10.

Table 2: Initial conditions for semi-analytic model comparison to data in Figure 16.

Model	t_0 (ms)	z_0 (km)	u_0 (10^2 km s $^{-1}$)	b_0 (km)	ρ_0 (10^9 g cm $^{-3}$)	g_0 (10^4 km s $^{-2}$)	$\rho_{f,0}$ (10^9 g cm $^{-3}$)
A0	50.59	50.61	2.37	7.83	2.30	3.57	2.50
AV	51.10	50.89	2.42	7.86	2.16	3.76	2.65

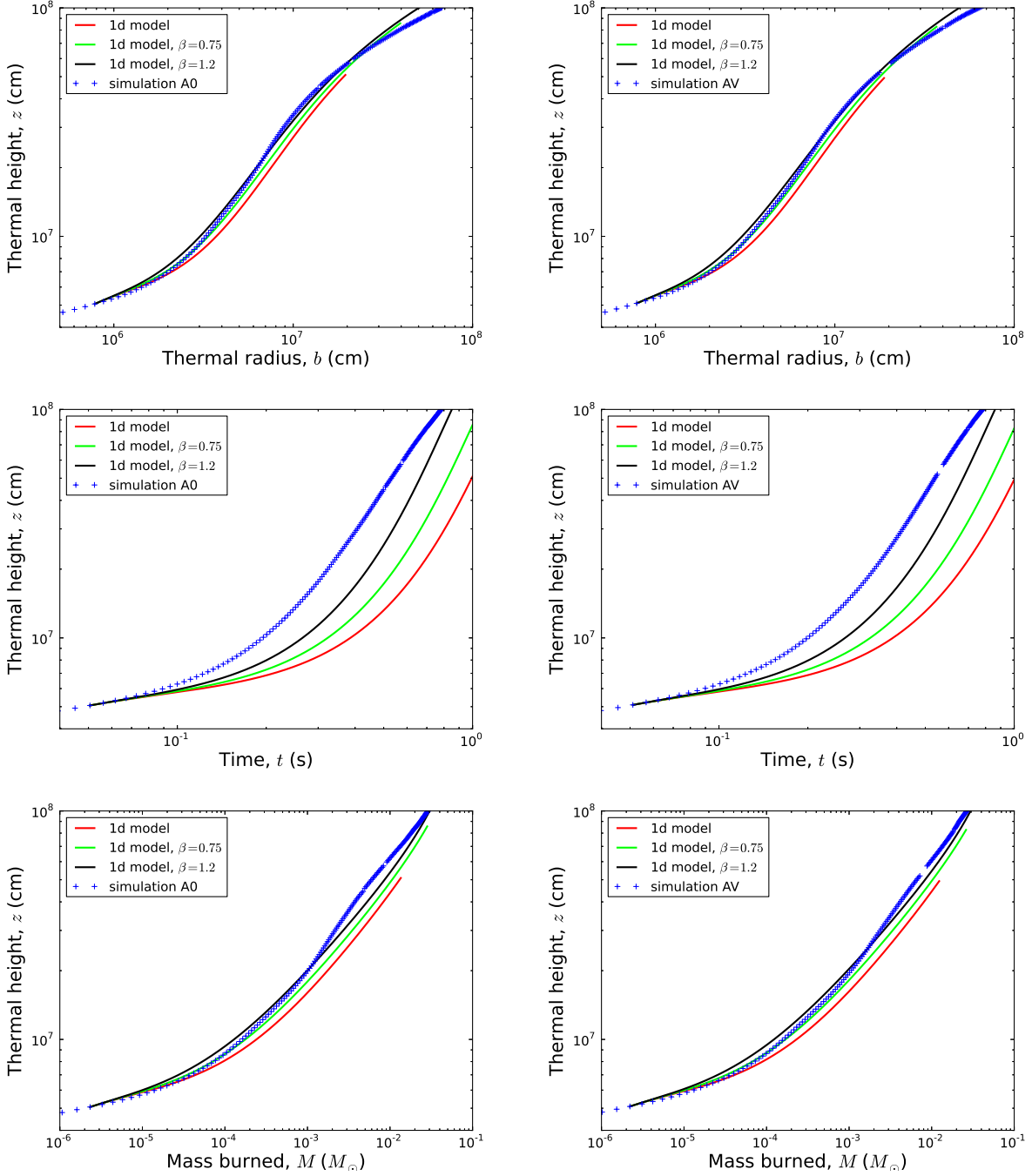


Fig. 16.— Comparisons of simulation data (crosses) with the semi-analytic one-dimensional model with various parametrizations (lines) for both Model A0 (left column) and Model AV (right column). In all cases, the semi-analytic model reproduces the general trend of the simulation data, but lacks sufficient buoyancy during the evolution.

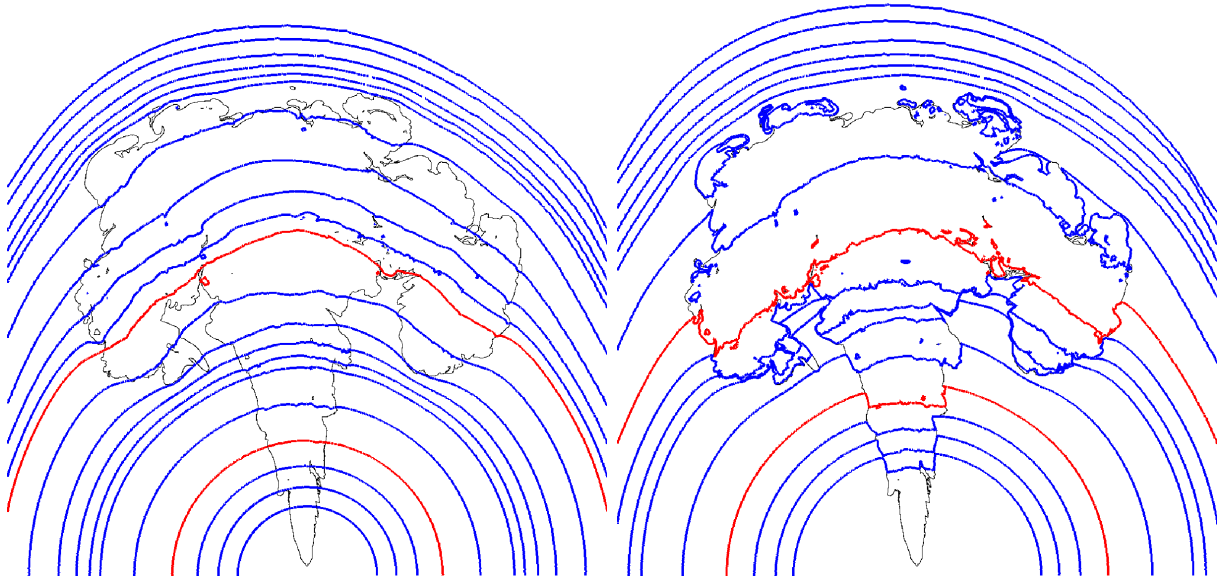


Fig. 17.— Pressure (left) and density (right) contours for Model AV at $t = 0.8\text{s}$. The thin black contour marks the flame surface. The red contours are highlighted to aid the eye. Each slice is 2400 km on a side. Deep in the star, where the pressure scale height is large, pressure contours lie on top of gravitational equipotentials, which are lines of constant radius. Equivalently, the lateral sound crossing time of the plume is short compared to the bubble rise so that pressure balance is maintained across the flame. At larger radii, the pressure scale height and sound speed decrease, while the bubble’s lateral extent and float speed increase. These changes lead to a situation where sound waves can no longer maintain pressure balance across the flame. Lateral pressure gradients form, which accelerate the lateral expansion of the flame.

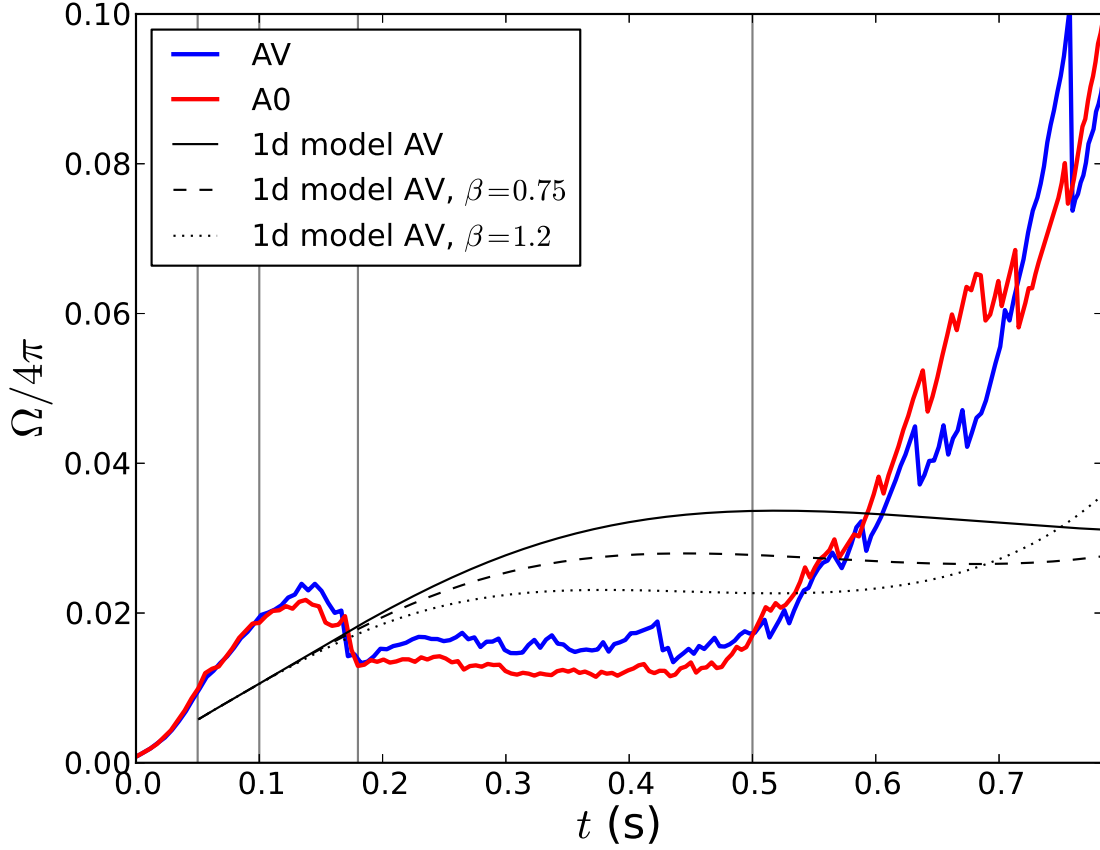


Fig. 18.— Solid angle of the bubbles as seen from the center of the star for Model AV (blue), Model A0 (red), and the one-dimensional semi-analytic model based on Model AV. The solid angle — after laminar burning through the initial perturbations — was $\Omega/4\pi = 4.4 \times 10^{-3}$. The thin grey lines mark the different stages in the bubble’s evolution as discussed in the text. Briefly, these phases can be delineated as: laminar burn, floatation, vorticity formation, transition to turbulence, and lateral expansion, from left to right.

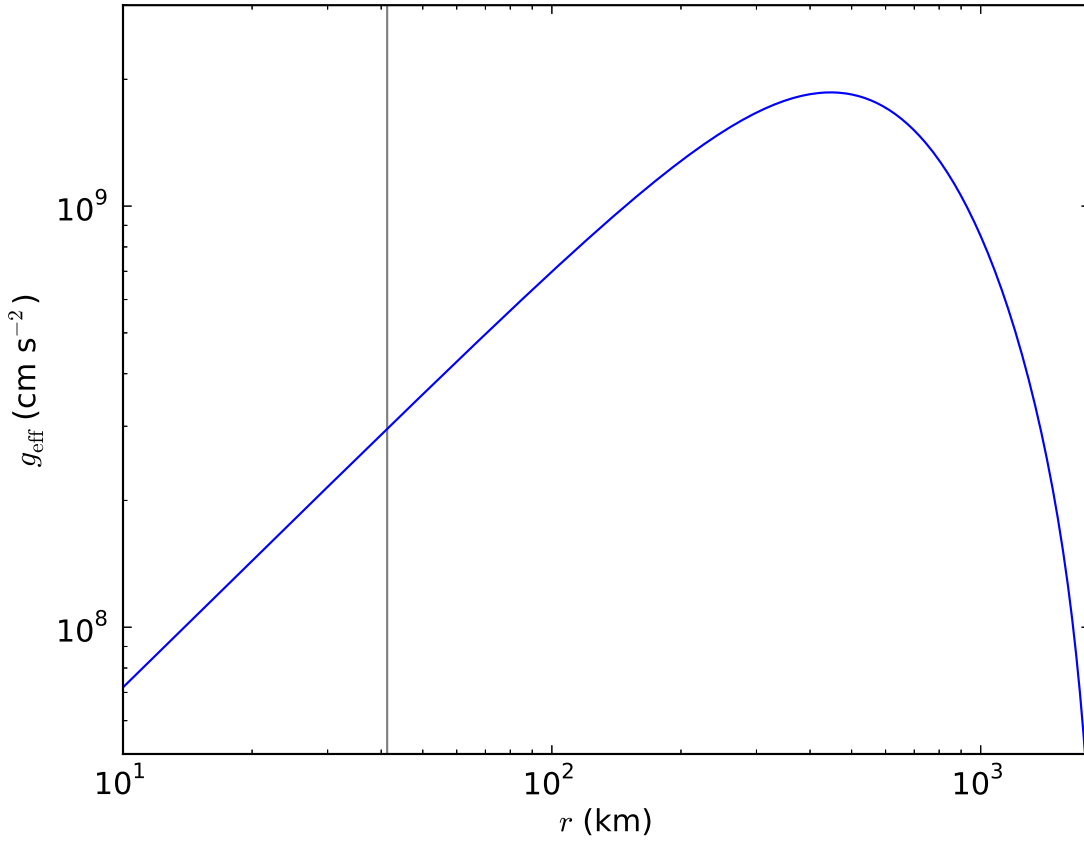


Fig. 19.— Effective gravity as a function of radius for our density profile and Atwood number determined from the flame data in Timmes & Woosley (1992). The grey vertical line marks the location of ignition for our model A runs. For radii less than about 300 km, $g_{\text{eff}} \propto r^{0.92}$; for larger radii, the decrease in density overcomes the increase in Atwood number, and g_{eff} plummets.

REFERENCES

- Almgren, A. et al. 2010a, Proceedings of SciDAC 2010, <http://computing.ornl.gov/workshops/scidac2010/papers.shtml>
- Almgren, A. S. et al. 2010b, *Astrophysical Journal*, 715, 1221
- Aspden, A. J., Bell, J. B., Dong, S., & Woosley, S. E. 2011, *ApJ*, 738
- Baraffe, I., Heger, A., & Woosley, S. E. 2004, *ApJ*, 615, 378
- Bell, J. B. 2013, BoxLib User’s Guide, <https://ccse.lbl.gov/BoxLib/>, [Online]
- Chamulak, D. A., Brown, E. F., Timmes, F. X., & Dupczak, K. 2008, *ApJ*, 677, 160
- Dong, S., Woosley, S. E., Malone, C. M., Almgren, A. S., & Bell, J. B. 2013, in prep.
- Gamezo, V. N., Khokhlov, A. M., & Oran, E. S. 2005, *ApJ*, 623, 337
- García-Senz, D., & Bravo, E. 2005, *A&A*, 430, 585
- Garcia-Senz, D., & Woosley, S. E. 1995, *ApJ*, 454, 895
- Höflich, P., & Stein, J. 2002, *Astrophysical Journal*, 568, 779
- Hillebrandt, W., Kromer, M., Röpke, F. K., & Ruiter, A. J. 2013, *Frontiers of Physics*, 8, 116
- Hillebrandt, W., & Niemeyer, J. C. 2000, *Annu. Rev. Astron. Astrophys*, 38, 191
- Jackson, A. P., Calder, A. C., Townsley, D. M., Chamulak, D. A., Brown, E. F., & Timmes, F. X. 2010, *ApJ*, 720, 99
- Jordan, IV, G. C., Fisher, R. T., Townsley, D. M., Calder, A. C., Graziani, C., Asida, S., Lamb, D. Q., & Truran, J. W. 2008, *ApJ*, 681, 1448
- Khokhlov, A. M. 1991, *Astronomy and Astrophysics*, 245, 114
- Khokhlov, A. M. 1995, *Astrophysical Journal*, 449, 695
- Kromer, M. et al. 2013, *MNRAS*, 429, 2287
- Krueger, B. K., Jackson, A. P., Calder, A. C., Townsley, D. M., Brown, E. F., & Timmes, F. X. 2012, *ApJ*, 757, 175
- Kuhlen, M., Woosley, S. E., & Glatzmaier, G. A. 2006, *ApJ*, 640, 407

- Livne, E., Asida, S. M., & Höflich, P. 2005, *ApJ*, 632, 443
- Ma, H., Woosley, S. E., Malone, C. M., Almgren, A. S., & Bell, J. B. 2013, *ApJ*, 771, 58
- Niemeyer, J. C., Hillebrandt, W., & Woosley, S. E. 1996, *ApJ*, 471, 903
- Nonaka, A., Almgren, A. S., Bell, J. B., Lijewski, M. J., Malone, C. M., & Zingale, M. 2010, *ApJS*, 188, 358
- Nonaka, A., Almgren, A. S., Bell, J. B., Ma, H., Woosley, S. E., & Zingale, M. 2011, Proceedings of SciDAC 2011, <http://press.mcs.anl.gov/scidac2011/agenda-2/scidac-2011-papers/>
- Nonaka, A., Aspden, A. J., Zingale, M., Almgren, A. S., Bell, J. B., & Woosley, S. E. 2012, *Astrophysical Journal*, 745
- Röpke, F. K., & Hillebrandt, W. 2005, *A&A*, 431, 635
- Reinecke, M., Hillebrandt, W., Niemeyer, J. C., Klein, R., & Gröbl, A. 1999, *A&A*, 347, 724
- Rendleman, C. A., Beckner, V. E., Lijewski, M., Crutchfield, W. Y., & Bell, J. B. 2000, *Computing and Visualization in Science*, 3, 147
- Röpke, F. K. 2007, *ApJ*, 668, 1103
- Röpke, F. K., Hillebrandt, W., Niemeyer, J. C., & Woosley, S. E. 2006, *A&A*, 448, 1
- Röpke, F. K., Hillebrandt, W., Schmidt, W., Niemeyer, J. C., Blinnikov, S. I., & Mazzali, P. A. 2007a, *ApJ*, 668, 1132
- Röpke, F. K., Woosley, S. E., & Hillebrandt, W. 2007b, *ApJ*, 660, 1344
- Schmidt, W., Niemeyer, J. C., & Hillebrandt, W. 2006a, *A&A*, 450, 265
- Schmidt, W., Niemeyer, J. C., Hillebrandt, W., & Röpke, F. K. 2006b, *A&A*, 450, 283
- Seitenzahl, I. R. et al. 2013, *MNRAS*, 429, 1156
- Timmes, F. X., & Swesty, F. D. 2000, *ApJS*, 126, 501
- Timmes, F. X., & Woosley, S. E. 1992, *Astrophysical Journal*, 396, 649
- Townsley, D. M., Calder, A. C., Asida, S. M., Seitenzahl, I. R., Peng, F., Vladimirova, N., Lamb, D. Q., & Truran, J. W. 2007, *ApJ*, 668, 1118

- Townsley, D. M., Jackson, A. P., Calder, A. C., Chamulak, D. A., Brown, E. F., & Timmes, F. X. 2009, *ApJ*, 701, 1582
- Woosley, S. E., Wunsch, S., & Kuhlen, M. 2004, *Astrophysical Journal*, 607, 921
- Wunsch, S., & Woosley, S. E. 2004, *ApJ*, 616, 1102
- Zhang, J., Messer, O. E. B., Khokhlov, A. M., & Plewa, T. 2007, *ApJ*, 656, 347
- Zingale, M., Almgren, A. S., Bell, J. B., Nonaka, A., & Woosley, S. E. 2009, *ApJ*, 704, 196
- Zingale, M., & Dursi, L. J. 2007, *ApJ*, 656, 333
- Zingale, M. et al. 2002, *Astrophysical Journal Supplement*, 143, 539
- Zingale, M., Nonaka, A., Almgren, A. S., Bell, J. B., Malone, C. M., & Woosley, S. E. 2011, *Astrophysical Journal*, 740

A. Isotropic Burn Flame Test Problem

We wanted to make sure that the flame was burning properly in all directions, such that the thermal diffusion was behaving isotropically for a given thermodynamic state. To that end, we set up a constant density ($\rho = 2 \times 10^9 \text{ g cm}^{-3}$), constant temperature ($T = 5 \times 10^8 \text{ K}$) atmosphere without gravity and added an ignition point of the same size as that used in the simulations presented in this paper. This problem was performed on 576^3 zones with a resolution of 100 m zone^{-1} .

We set up two different initial conditions for the shape of the ignition spot as shown in the slices of Figure 20. The perturbed sphere in the left plot has the same shape and size as that used in the simulations presented in this paper; the ignition spot in the right plot is a perfect sphere, given our resolution. Each of the contours marks where $X(^{12}\text{C}) = 0.45$, and they are separated by 0.01 s of evolution with the initial conditions shown as the central contour. Indeed, there is no preferred direction to the flame propagation, and the initial perturbations are burned through very quickly, as is the case in the main simulations of this paper (e.g. Figure 3). The constant flame speed used in this test problem was set low so that the flame moved at the minimum speed, the laminar speed, $v_l = 76 \text{ km s}^{-1}$ at this density. The distance between contours in these plots should then be 760 m, which is consistent with the results of the test problem.

B. Galilean Invariance of the Flame

The stem of the flame experiences a strong crosswind — the bulk velocity in the vicinity of the flame’s stem is nearly parallel to the flame surface, whereas the flame propagates normal to its surface. We wanted to check that this crosswind was not affecting the propagation of the flame in an unexpected manner; we wanted to make sure the flame propagation was Galilean-invariant. This problem was performed on a 128×1024 grid.

We used the same initial background conditions as in Section A: constant density ($\rho = 2 \times 10^9 \text{ g cm}^{-3}$), constant temperature ($T = 5 \times 10^8 \text{ K}$) atmosphere in the absence of gravity. We isobarically turned the left 30% of the domain into hot ash; the initial conditions are shown as the upper left panel in Figure 21. The lower x boundary condition was set to a symmetry wall, and the upper x and y boundaries were set to outflow. At the lower boundary, we inject the same initial composition profile with a velocity, $\vec{v}_{\text{in}} = (0, v_{\text{in}})$, with the inflow speed v_{in} a free parameter. In steady-state, a Galilean-invariant flame surface should constitute a line with slope v_{in}/v_f , with the limiting case of no inflow being a vertical line.

Figure 21 shows in the top right the ^{12}C mass fraction of a pure laminar ($v_l = 76 \text{ km s}^{-1}$) flame with no cross wind. The bottom two panels experience a $v_{\text{in}} = 500 \text{ km s}^{-1}$ cross wind with the left panel using the laminar speed and the right panel using $v_f = 100 \text{ km s}^{-1}$. All panels are at about the same time, when the flame first hits the right wall in the laminar case. Note that in the bottom left panel, the flame also first touches the right wall at this time, but it occurs off the top of this panel; the images were cropped to keep the aspect ratio manageable. Excepting an initial transient and adjustment at the inflow boundary, the flames trace a straight line. The black lines in the bottom two panels show the expected behaviour with slopes of $5/0.76$ for the left and 5 for the right.

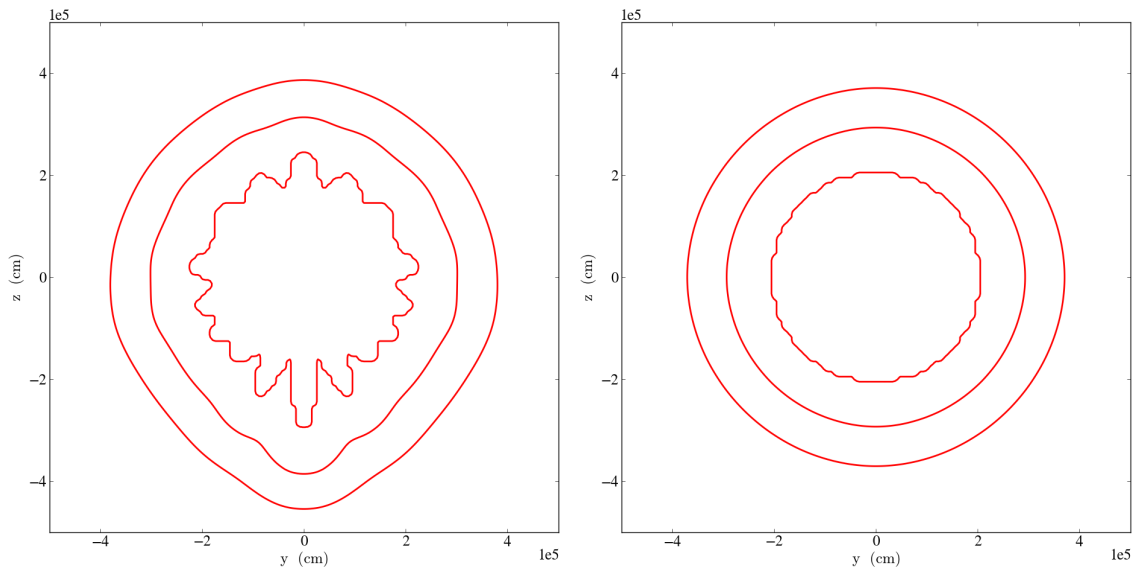


Fig. 20.— Isotropic burn test problem for two different initial conditions — perturbed sphere (left) and sphere (right). Each of the contours marks the $X(^{12}\text{C}) = 0.45$ isocontours at $t = 0, 0.01,$ and 0.02 s, with the initial conditions being the central contour. The spacing between contours is consistent with the laminar speed used to move the flame, $v_l = 76 \text{ km s}^{-1}$.

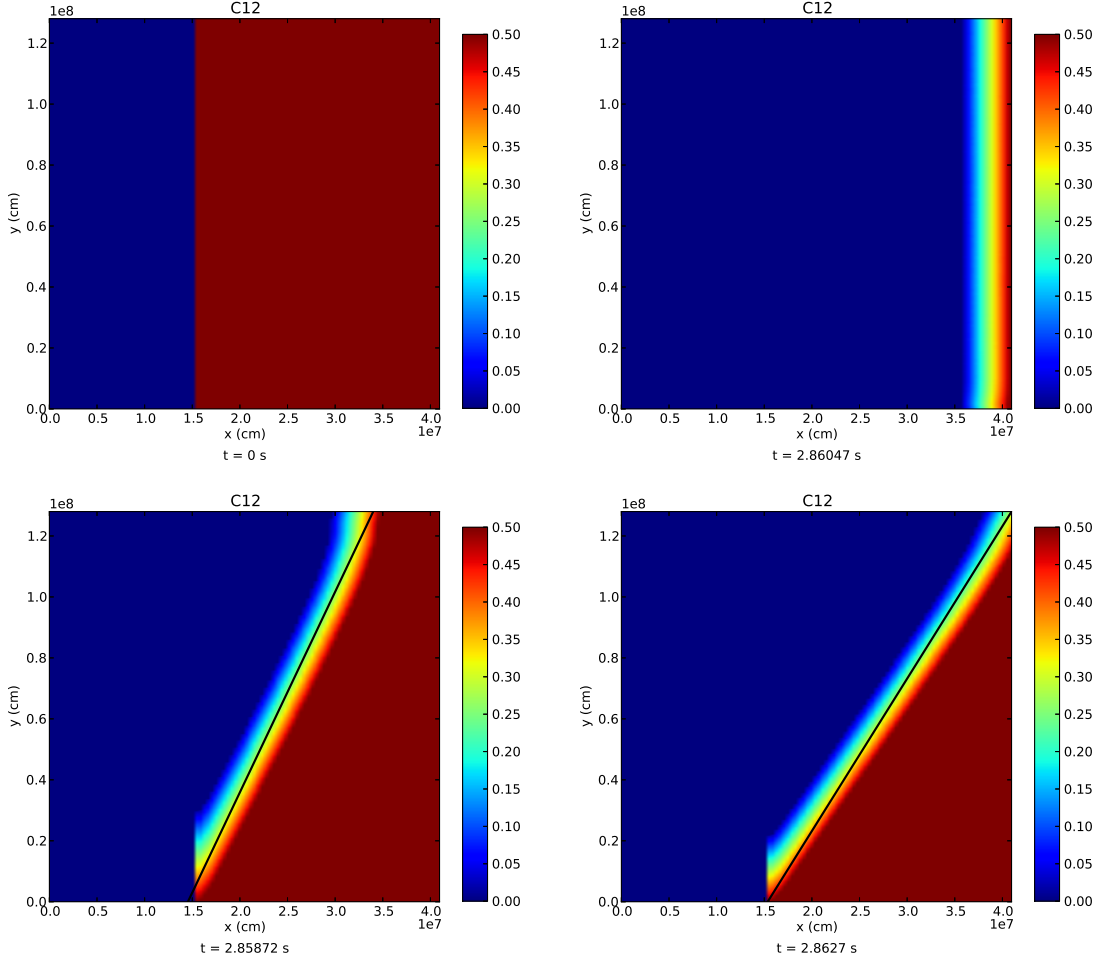


Fig. 21.— Galilean invariance flame test problem. Color maps show the ^{12}C mass fraction, with the top left panel showing the initial conditions. The boundary conditions are such that the initial composition is inflowing through the bottom at speed v_{in} and the flame is burning to the right at speed v_f . The top right panel is for $v_{\text{in}} = 0$ and $v_f = v_l = 76 \text{ km s}^{-1}$, i.e. laminar flame with no cross wind.. The bottom two panels have $v_{\text{in}} = 500 \text{ km s}^{-1}$, with the left panel using $v_f = v_l$ and the right $v_f = 100 \text{ km s}^{-1}$. The black lines in the bottom panels show the expected steady-state slope of the flame-ash interface. Neglecting curvature effects from the inflow boundary condition, the expected behavior is very nearly reproduced.